NUMERICAL SIMULATION AND MECHANICAL PROPERTIES OF FREE-STANDING SILVER THIN FILMS

Except where reference is made to the work of others, the work described in this thesis is my own or was done in collaboration with my advisory committee. This thesis does not include proprietary or classified information.

_____

Feng Qian

Certificate of Approval:

_____	_____
Bryan Allen Chin Professor Materials Engineering	Barton C. Prorok, Chair Assistant Professor Materials Engineering
_____	_____
Dong-Joo Kim Assistant Professor Materials Engineering	Stephen L. McFarland Acting Dean Graduate School

NUMERICAL SIMULATION AND MECHANICAL PROPERTIES OF FREE-STANDING SILVER THIN FILMS

Feng Qian

A Thesis

Submitted to

the Graduate Faculty of

Auburn University

in Parital Fulfillment of the

Requirement for the

Degree of

Master of Science

Auburn, Alabama
December 15, 2006

NUMERICAL SIMULATION AND MECHANICAL PROPERTIES OF FREE-STANDING SILVER THIN FILMS

Feng Qian

_____
Signature of Author

_____
Date of graduation

THESIS ABSTRACT

NUMERICAL SIMULATION AND MECHANICAL PROPERTIES OF FREE-STANDING SILVER THIN FILMS

Feng Qian

Master of Science, Dec 15, 2006
(B.E. Nangjing Unviersity of Aeronautics and Astronautics, Nanjing, China, 2003)

97 Typed pages

Directed by Bart Prorok

Membrane deflection test is well studied to investigate the mechanical properties for polycrystalline metal thin films. Numerical simulations by ANSYS software of membranes with different bottom window sizes show the overestimation of elastic modulus while using the gauge width to calculate the elastic modulus. The second part of the work includes the fabrication and membrane deflection test of 0.5 μm and 1μm silver free standing thin films. Two methods to etch silicon nitride to release the silver membranes are performed by using inductively coupled plasma (ICP) etcher STS AOE (Advance oxide etcher) and by hot phosphoric acid etching. The mechanical behavior of silver free-standing thin films released by AOE and hot acid etching show a discrepancy. It may be contributed to the texture change due to heat treatment of silver thin film during hot phosphoric acid etching. Also shear localization is observed in the deformation process of silver thin film with hot phosphoric acid etching.

ACKNOWLEDGEMENTS

It's a genuine pleasure for me to take this opportunity to acknowledge people due to which this work was done to my contentment and in an atmosphere I cherished. I expressed my sincere gratitude to my advisor, Dr. Bart Prorok who provided support, guidance and personal attention which I consider unparallel to find in graduate study. His timely motivation and encouragement to pursue my own ideas gave me unique experience which is difficult for any graduate student to accomplish, for which I am very thankful.

I would like to thank my group mates Liwei, Wang for her patient help on teaching enormous experimental skills and worked with me whenever I need her most. Also I am thankful to Shakib Morshed for his great help on teaching me invaluable knowledge of microfabrication as well as hands-on experiences. I would also like to thank my group mates Bo Zhou, Cai Liang, Nicole Harris for their support and help. I am thankful to Charles Ellis of AMSTC in Auburn University for giving me suggestions and pointers during microbraction hick-ups.

I am grateful to L.C Mathison for his support as well as great encouragement for this work. Finally I would acknowledge the most important people, my parents without whom I would not have completed this work. The motivation and help from my patents who always stood by me during times when things were rough was really helpful for this work.

Style manual or journal use IEEE

Computer software used Microsoft Office 2003.

TABLE OF CONTENTS

LIST OF FIGURES

LIST OF TABLES

CHAPTER 1

INTRODUCTION

1.1 Overview

Polycrystalline metal thin films have a wide variety of applications in the microelectronics and MEMS (Microelectromechanical System) devices, such as microsensors, optical devices and magnetic storage media, and protective or decorative coatings. In these applications, not only the functional properties of thin films (e.g. electrical, optical, and magnetic properties) but also the mechanical properties affect the devices' performance and durability. Mechanical demands placed on thin films in these applications can lead to various failures because of the plastic deformation, stress-induced cracking, etc. in the films. However, most of our knowledge in these areas is based on the knowledge of the mechanical behaviors of bulk materials, which most often is insufficient and misleading to explain mechanical responses of the materials in this size regime. Therefore, to realistically and precisely predict the occurrence of those types of failure, a thorough and clear understanding of the inelastic behavior of thin films is necessary and also critical.

Limitations of materials reliability and failure are frequently due to thermal and intrinsic stresses, fatigue or diffusion. In this context the microstructure of thin films plays a key role. Especially the texture, grain size distribution, grain morphology and

spatial distribution of the grain orientations are the most important microstructural characteristics which influence the mechanical properties. [1-3]

As the thin film dimensions begin to approach the scale of the material microstructure features, the mechanical properties of materials tend to exhibit a critical dependence on the specimen size. For polycrystalline metal thin films, sometimes this size effect causes plastic yielding occurs at higher stresses than their bulk counterparts.

1.2 Thesis Structure

Chapter 2 gives a literature review of the methods for measuring the mechanical properties of thin films. Bulge test, which is designed to determine the in-plane mechanical properties of the film by eliminating specimen edge effects as well as avoiding the complexities from substrate material, is discussed. Electrostatic grip system and some other common testing methods are also discussed. Membrane deflection experiment (MDE), which was used in this study, is discussed then. The size effect of metal thin films is discussed and the Ashby modeling is supplied to explain the size-dependent phenomena. The common FCC metals are discussed based on their anisotropic properties and stacking fault energy.

Chapter 3 gives the design and the parameters of the specimens. Relationships between fringe distance and strain for small angel regions and large angel regions are calculated. Stress-strain curve can be generated based on the Cauchy stress converted from the nanoindenter vertical load and also the strain calculated from distance between interference fringes. Simple analytical solution is supplied to examine the errors due to our simplification of the geometry in calculations. Finite element analysis and ANSYS

software have been introduced and simulation results of 9 specimens by Solid45 model and Shell63 model are listed.

In Chapter 4, the experimental procedures including lithography, advanced oxide etcher, E-beam evaporation, lift off process and wet etching are discussed respectively. Also the experimental setup and test methodology of membrane deflection test is discussed.

In Chapter 5, the surface of silver thin films has been characterized by scanning electron microscopy (SEM). Larger gain growth is observed for the films after hot phosphoric acid etching. The possible reason is proposed. The experimental setup and the procedures as well as data reduction are described in detail. The membrane deflection tests of 0.5 μm and 1.0 μm free-standing silver thin films are performed. The stress-strain curves have shown the mechanical behavior of free-standing silver thin films.

Chapter 6 provides conclusion and future work.

CHAPTER 2

LITERATURE REVIEW

2.1 Testing Methods

Accurate knowledge of the nanoscale mechanical properties of thin films is important to the design and operation of Integrated Circuits (IC's), thin film optics, MEMS, and nanoscale devices. Although testing of bulk materials, and therefore bulk mechanical properties are well established, the properties of materials at nano/micro scale are not well known. Mechanical characterization of thin films presents numerous challenges, including length scale effects, the effect of native oxides, residual/intrinsic stresses, and the mechanical complexities of nanoscale layers of thin films. Experiments for measuring the mechanical properties of thin films fall into two key categories: films on a substrate or freestanding thin films. Typically, thin films are deposited on a substrate in their in-service location. Therefore, testing of thin films located on a substrate seems appropriate for determining the in-service mechanical properties. However, measurements made on such films are clearly influenced by the substrate. Thus, these measurements yield mechanical properties of a composite structure not of the thin film itself, especially for increasingly thinner sub-micron films. In order to obtain directly the properties of the thin films, it becomes necessary to test freestanding thin films.

Depth sensing indentation is a widely used method for estimating the mechanical properties of materials. It employs high-resolution instrumentation to continuously control and monitor the loads and displacements of an indenter as it is driven into and withdrawn from a material. The result is a load-displacement relationship with loading and unloading segments that describe material response. This technique is most frequently used to measure the hardness, but mechanical properties such as elastic modulus, yield stress and even the fracture toughness can also be evaluated from the same depth sensing indentation data with the incorporation of other tools [4, 5]. During the past two decades while the depth sensing indentation testing technique has been developed largely, there have been some successful results reported by many well-reputed experimental groups. Among them, indentation size effects attract more and more attention in this area; however, there are still points of controversy in interpreting this type of size effects from the indentation data due to the complication of the data reduction and extra effect induced by the substrate [6-8].

2.1.1 Bulge Test

One of the bending tests called bulge test, developed by Beams et al in 1959 [9] is designed to determine the in-plane mechanical properties of the film by eliminating specimen edge effects as well as avoiding the complexities from substrate material .As shown in figure 2.1, in the bulge test, a freestanding film is deflected by applying pressure with compressed gas or liquid. The film is fixed at the edges of the chamber, and the chamber is pressurized in a controlled manner that results in the freestanding film bulging upward. The resulting “bulge” height can then be measured by interferometry

and other techniques. The apparatus required to perform a bulge test is simple and the method is an easy way to examine both elastic and plastic properties. However, sample preparation is restricted to thin films with tensile residual stresses. Films with compressive residual stresses can buckle, which might cause underestimation of material properties [10, 11].

Both the depth sensing indentation and bulge test can all be categorized to methods that subject the specimen to gradients of strain, which at the micro/nano scales can complicate the extraction of material property from tested data. Also their flexibility for testing specimens of various geometries is limited. Alternatively, tensile testing is the most direct method for obtaining a material's mechanical properties due to its direct and independent measurement of loads and strains. Therefore, inspired by the tensile test performed on bulk samples, several micro-scale tensile testing systems have been established by the researchers.

2.1.2 Micro Tensile Test

Tsuchiya et al. developed a testing procedure employing electrostatic force gripping system to load the film. The specimen is fabricated as a freestanding thin film cantilever fixed at one end and with a large pad at the other end. Schematics of the architecture and gripping process are shown in figure 2.2. After fabrication and release of cantilever specimen, a probe is aligned and brought into contact with the specimen's free end to be gripped. An electrostatic attractive force is generated between the two surfaces with an applied voltage. This force is rather large compared to the force required to deform the specimen in tension; therefore, the two surfaces remain rigidly fixed together as long as

the voltage is applied. Tensile testing is then achieved through piezoelectric actuation of the probe along the axis of the specimen with displacements measured by a strain gauge at the probe. Specimen dimensions in the gauged region are on the order of 30-300μm for length, 2-5μm for the width, and 0.1-2.0μm for the thickness [12].

Ruud et al used motor driven micrometers to produce elongation in the free-standing films, and the load cell as well as laser diffraction technique to read the force and displacement, respectively [13]. The force resolution of the setup is 2mN, and we can test specimens with dimensions of 1 cm $\times$ (3.3-0.013)mm $\times$ (1.9-2.6)μm. Greek and Ericson et al developed a technique for *in situ* testing in a SEM using strain gauge type for sensors and optical linear encoder type displacement sensors [14]. They used the dry etching technique to prepare polysilicon specimens with a 10×10 μm^2 cross-section.

Chasiotics and Knauss have developed a tensile testing technique using electrostatically assisted ultraviolet (UV) adhesive gripping and they have tested specimens as thin as 1.9 um *in situ* in an AFM.

Another type of the microscale tensile test also employs the cantilever architecture, but it uses a ring at the free end. A probe with a diameter just smaller than the inner diameter of the ring is inserted and then pulled in the direction of the specimen axis to apply direct tension. An optical encoder is used to independently measure displacement. A problem with this test is the difficulty of eliminating friction between probe and substrate; therefore causing the data reduction procedure complicate.

Finally, there is this noteworthy and very promising microscale tensile test, called the membrane deflection experiment (MDE), which was developed by Espinosa and his co-workers. It involves the stretching of freestanding, thin-film membranes in a fixed-

fixed configuration with submicron thickness. In this technique, the membrane is attached at both ends and spans a micromachined window beneath. A nanoindenter applies a line-load at the center of the span to achieve deflection. Simultaneously, an interferometer is focused on the bottom side of the membrane to record the deflection. The result is that direct tension is involved, in the absence of bending and strain gradients of the specimen [15-17]. Detailed description about the methodology of this technique is shown in chapter 3 & 4.

2.1.3 MEMS Based Test

Saif and MacDonlad used an electrostatic comb drive actuator to fracture a silicon oxide composite specimen with a cross-section of 1×1 μm^2. As in figure 2.3, the specimen is co-fabricated with the actuator, which enables precise alignment and gripping of the specimen and also reduces the setup size[18]. Sharpe et al. developed a technique for tension of polysilicon specimens as thin as 1.5 μm [19]. A piezoactuator is used to generate the displacement in the specimens. Strain and stress in the specimens are measured by capacitive displacement sensors and load cells, respectively. The piezoactuated tensile testing apparatus developed by Read et al., shown in Figure 2.4, was also used to test microscale free standing specimens [16].

The method of microcantilever beam bending was developed by Wiehs et al. who demonstrated the technique on a 0.87μm-thick gold film. A nanoindenter was used as the loading device. The bending test setup for nanoscale thin films requires more stringent force resolution compared to the tensile testing, and the spring constant of the loading system must be comparable to that of the microcantilver specimen.

2.2 Size Effect of Polycrystalline Metals

Several pioneering studies have been done to experimentally identify the existence of size effect on plasticity of polycrystalline metals. One of them is reported by Fleck et al. in 1994 about the strengthening effect resulted from decreasing the diameter of thin metal wires in a micro-torsion test. In this test, a torque was applied on copper rods with varying diameters in the range of 12-170μm. And an increase in strength by a factor of two or three for the smallest wire over the largest was observed. Direct tensile tests were also performed on those copper wires which have identical structure size. The authors concluded that for the most part, no size effect existed while those wires subjected to direct tension [20].

Another similar micro-bending test has been performed by Stolken and Evans in 1998, in which bending strips of metals with different thickness around a rigid rod were designed. The strips varied in thickness from 12, 25, to 50 μm and each was bent around a rigid rod whose diameter scaled with film thickness to ensure identical states of strain in each strip. The result showed clearly that as each strip was strained to the same degree the thinner strips required a larger bending moment [2]. Moreover, micro- and nano-indentation tests have proven a strong size effect as shown that the material hardness decreases as indentation depth increases by a factor of two to three [3, 21, 22]. Besides, indentation of thin films also shows an increase in the yield stress with decreasing the penetration depth [23]. There are many other noteworthy mechanical problems that show strong size effects. One is called Hall-Petch behavior, which describes that both yield stress and hardness of tested polycrystalline materials increases with decreasing the grain size. Other size effects in fracture are found when the fracture toughness K_{IC} in the

fracture design codes decreases with increasing thickness; the yield stress increases with decreasing of the size of the process zone ahead of a crack tip; increase in strength with decreasing the size of the notch for U-notched geometrically similar ensile bars, etc. All of these studies have shown strong size effect that strength increases with decreasing structure size at micron and submicron scales. The mechanical properties of polycrystalline metallic materials, such as yield stress and hardness, as well as fracture are size dependent whether in simple torsion, bending, or indentation testing.

In these pioneering size effect studies, the size dependence of the mechanical properties was considered generally to be a result of non-uniform straining. Figure 2.5, shown as below, is a logarithmic length scale figure beginning at the atomic scale and ending at the macro scale. On the left are four categories of structures and the regimes where their dimensional size fits on the length scale. On the right are regimes indicating where dimensional size effects begin to affect the material mechanical properties and the theories used to interpret behaviors.

It was known that the classical continuum plasticity cannot predict the size dependence in this regime. The generally accepted size limit for accurate description of plasticity by the classical theory is the system with dimensions greater than approximately 100 μm. On the other hand, it is still impossible to perform quantum and atomistic simulations to describe material behavior for more than one million atoms by molecular mechanics. The maximum size regime computationally approachable is the system with dimensions less than 0.1 μm. This leaves an intermediate gap between the classical continuum theories and molecular dynamic simulations.

During the past several decades, a number of scientists have argued if the size dependence of the material mechanical properties results from an increase in strain gradients inherent in small localized zones which lead to geometrically necessary dislocations that are responsible for the additional hardening [24-27]. Material deformation in metals enhances the dislocation formation, the dislocation motion, and the dislocation storage. The dislocation storage causes material hardening. The stored dislocations generated by trapping each other in a random way are referred to as statistically stored dislocations; while some extra dislocations accumulated in addition to statistically stored dislocations to accommodate the strain gradient are named geometrically necessary dislocations. Statistically stored dislocations are believed to be related to the effective plastic strain, while the density of geometrically necessary dislocations is proportional to the gradient of the effective plastic strain [1, 28, 29]. Therefore, inspired by the aforementioned size effect studies, a couple of gradient-induced strengthening theories have been proposed to explain and predict this size dependency of materials at micron and submicron regimes. Some of these theories did succeed in explaining size effect with the incorporation of an intrinsic material length parameter into the modeling. However, the difficulties resulting from both experiments and analysis to determine the intrinsic material length limited the fully understanding and their applications of the plasticity gradient strengthening mechanisms.

In the aforementioned Fleck's work, direct tensile tests were also performed on identically sized copper wires. The authors concluded that for the most part, no size effects existed for this case [20]. It should be mentioned that the smallest rod diameter investigated by this group was 12 μm. The homogeneous manner in which uni-axial tests

were conducted seems to have hindered the occurrence of gradients in plasticity. The question then turns into whether size effects can exist in the absence of strain gradients. Recent work on tensile testing of gold thin films with submicron thickness has shown that size effects do indeed exit in the absence of strain gradients. In these studies, grain size was held constant at approximately 250 nm while specimen thickness and width were varied systematically. Experimental results showed that the yield stress more than doubled when film thickness was decreased. For the thinner specimens, a brittle-like failure exhibited and a strain softening behavior occurred for the thicker ones [15, 17]. It is believed that these size effects result from the limited number of grains through the thickness, which limits the number of dislocation sources and active slip systems. Therefore, other deformation modes such as grain rotation and grain boundary shearing accompanied by diffusion become dominant.

Although there has been an extensively tremendous theoretical and experimental work done to understand the size dependency behavior of materials, this area is still in its critical state with numerous controversies. Future investigations are more than necessary to address the insight of the fundamental mechanisms about materials deformations at this scale.

The greatest challenge in investigating the size effect phenomenon is performing mechanical tests for determining stress-strain behavior. Since the physical dimensions of specimens range from a few hundred micrometers down to as small as 1.0 nanometer, novel mechanical testing methods have been developed to measure their properties.

2.3 Deformation Modeling

M. F. Ashby proposed a polycrystalline materials deformation model in the late 1960s, which was originally used to explain the grain-size-dependent phenomena [29]. However, four decades later, we are still inspired by the way how he clarified the movement and incorporation of individual grains under deformation with respect to each other; and would like to use his concept as fundamental bricks to establish a realistic model to explain plasticity size effects by integrating with the microstructure information especially the grain orientation data from EBSD patterns as well as the stress-strain signatures of the tested specimens.

Figure 2.6 briefly illustrates the theory behind the Ashby model, one of the biggest assumption is to separate the deformation of each grain into a uniform deformation, and a set of local, non-uniform deformation. First, each grain is considered to undergo a uniform tensile strain. A result of overlapping and voiding in between the individual grains occurred like shown in figure 2.6 (b). And at this stage, only statistically stored dislocations had been generated to response. After that, the grains were treated as they underwent a non-uniform deformation as illustrated in figure 2.6 (c). In this part, the overlapping created by the first stage can be corrected by shear displacements, introducing local shear by running dislocations in from the boundary. While voids can be compromised by the same process, using dislocations of opposite sign. The dislocations involved in this stage are geometrically necessary, whose density was expressed as $\rho^G \cong \frac{\bar{\varepsilon}}{4bD}$ where b is the magnitude of the Burgers vector; D is the average grain size

and $\bar{\varepsilon}$ can be related to the amount of overlap or void occurred. And the final arrangement of those grains under such a tensile load is shown in figure 2.6 (d).

2.4 Materials Selection

This work will investigate the thin film mechanical response of several FCC metals, illustrated in Figure 2.7. Most of them are materials that have been widely employed in the manufacturing of microelectronics and MEMS devices.

Table 2.1 lists the anisotropic ratio and stacking fault energy for those materials. The stacking fault energy is an important parameter to determine how a material deforms. FCC metals deform predominantly by crystallographic slip. This is the case for materials with high stacking fault energy. However, the low stacking fault energy materials like silver enable deformation twinning to play an increased role beside the crystallographic slip in plastic deformation [30]. In addition to the differences in stacking fault energy, these FCC metals also have different degree of anisotropy in linear elasticity. Table 2.1 also gives the elastic modulus of FCC metals for different direction and polycrystalline cases.

A polycrystalline material exhibits elastic isotropy due to averaging out over a large number of randomly oriented grains. However, in the form of thin film, polycrystalline material will exhibit a preferred crystallographic texture leading to their anisotropic property instead of averaging out. Take aluminum and gold as examples, the elastic modulus of aluminum exhibits a small degree of elastic anisotropy and varies from 64 to 76 GPa; while silver exhibits a large anisotropy with modulus varying from 44 to 120 GPa. Thus, depending on the film's texture, the elastic deformation of silver will vary

significantly while that of the aluminum can remain relatively unchanged. Also the higher value of anisotropic ratio for silver indicates its ability to deform by deformation twinning in addition to crystallographic slip [30]. Therefore, the anisotropy ratio is also expected to plays a part in the size effect phenomenon. English and Chin plotted the ratio of <100> to <111> for various FCC materials as a function of stacking fault energy (SFE). Silver had the largest <100> to <111> among these FCC materials they have examined. For materials with higher SFE than silver, the <100> to <111> ratio decreased with increase of SFE. They claimed that the mechanical twinning enhanced the <100> orientation with decreasing SFE in the region of higher SFE compared with that of silver, and latent hardening enhanced <111> component at the expense of the <100> component in the region of lower SFE.

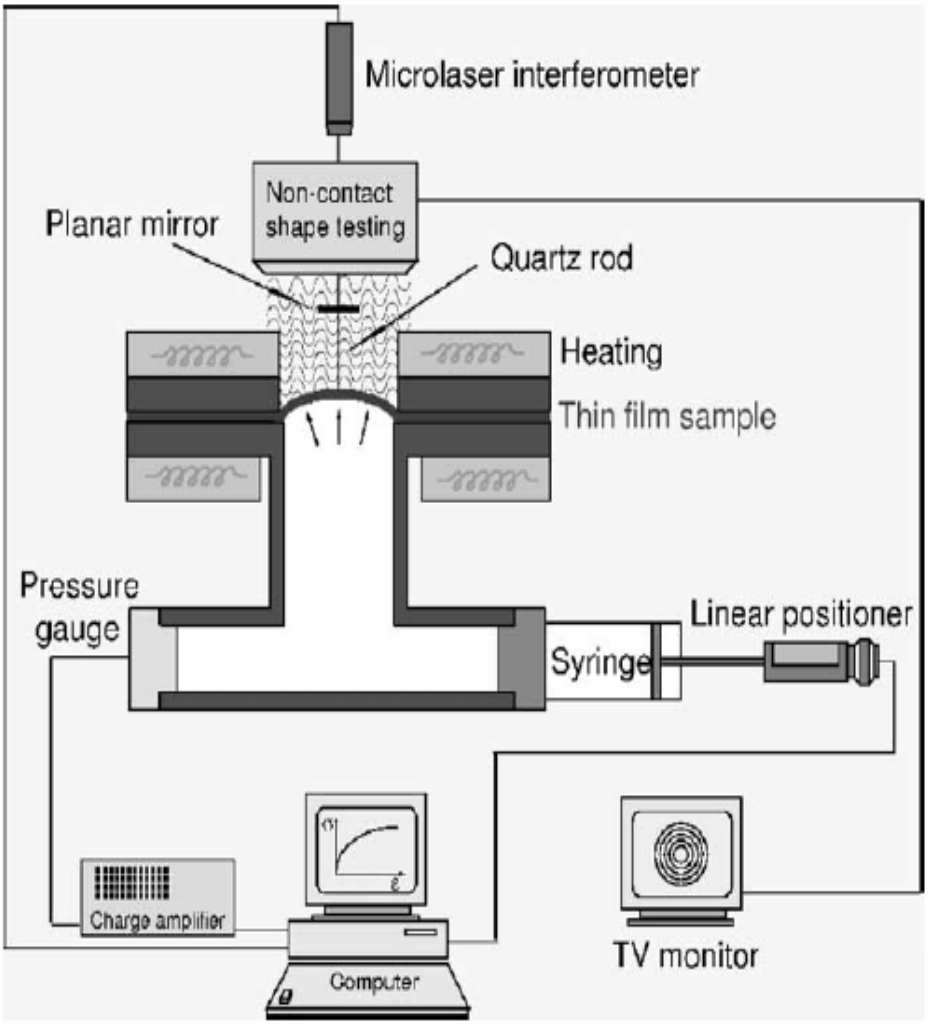

Figure 2.1 Schematic diagram of a bugle test device [9].

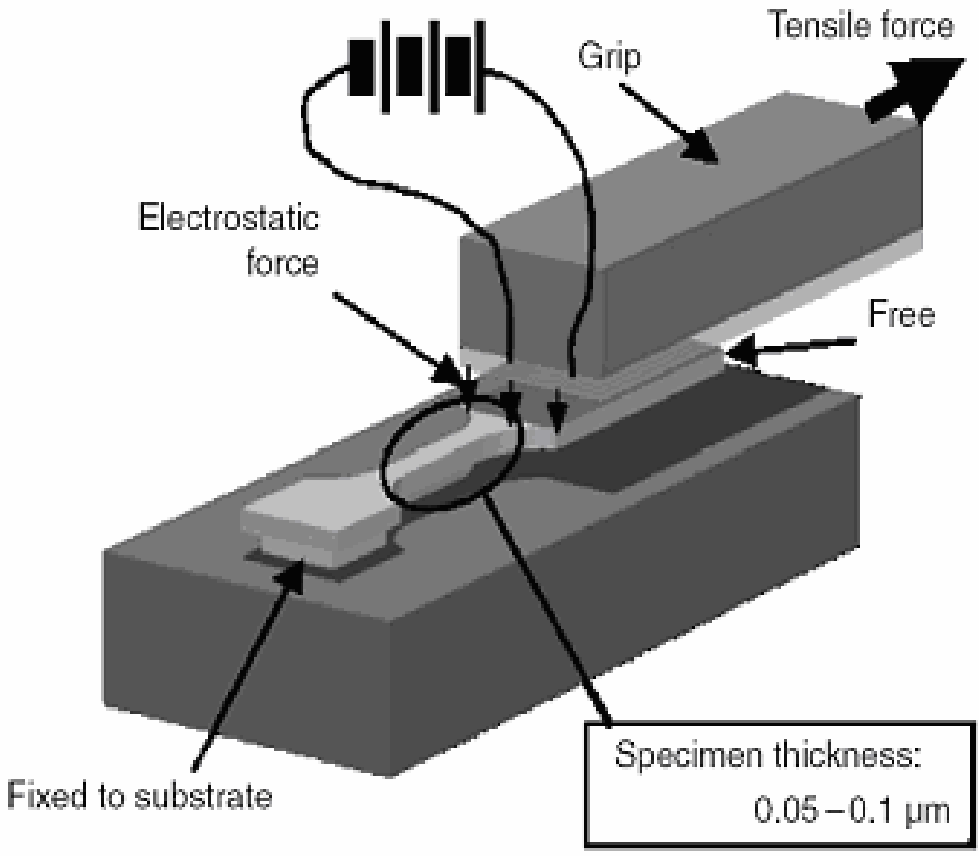

Figure 2.2 Schematics of the architecture in the electrostatic grip system [12].

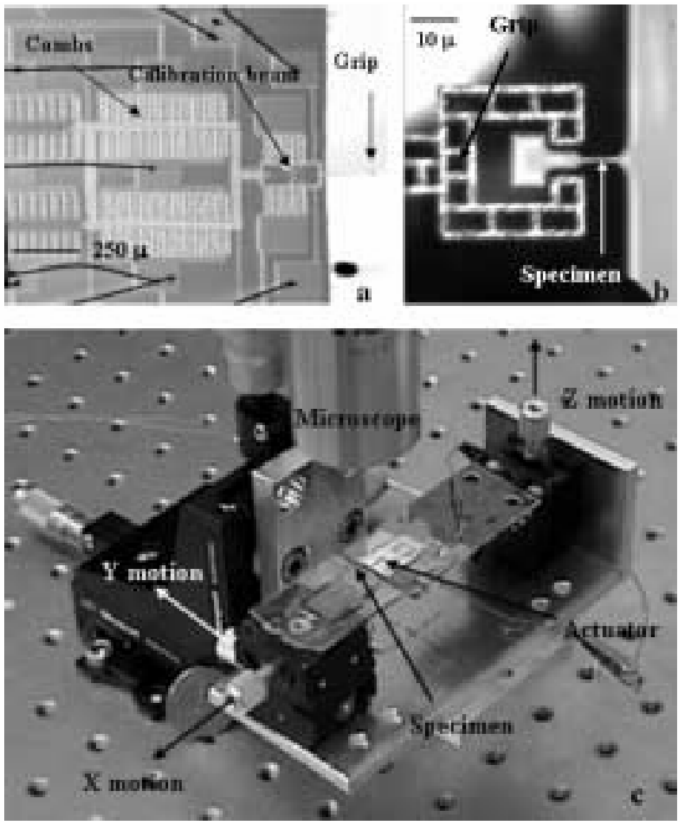

Figure 2.3 A MEMS-based tensile testing setup: (a) the electrostatic comb drive actuator; (b) zoomed view of the specimen and the actuator grip; (c) the experimental setup (note that the black three-axis positioner is not a part of the setup) [18]

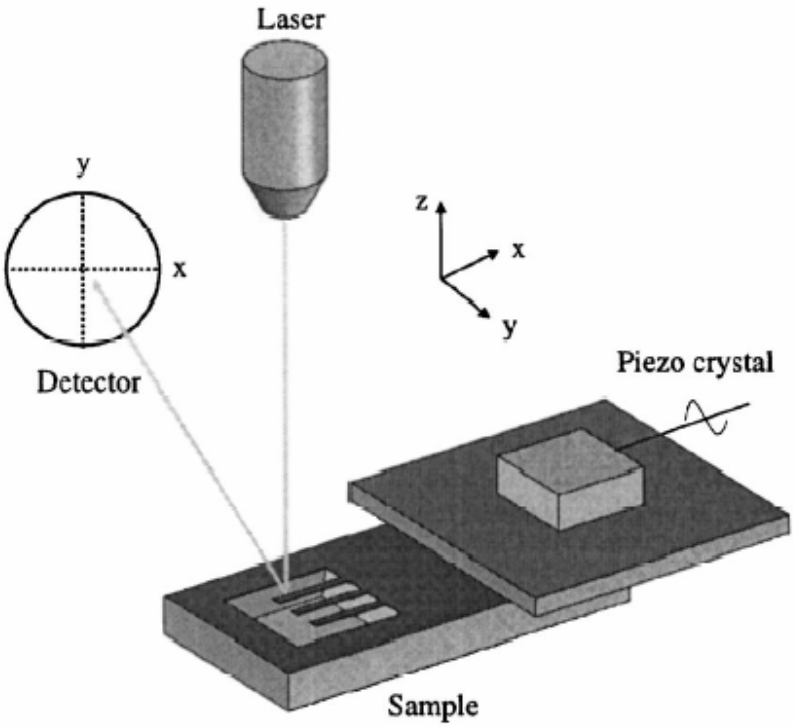

Figure 2.4 The piezoactuated tensile testing apparatus [16]

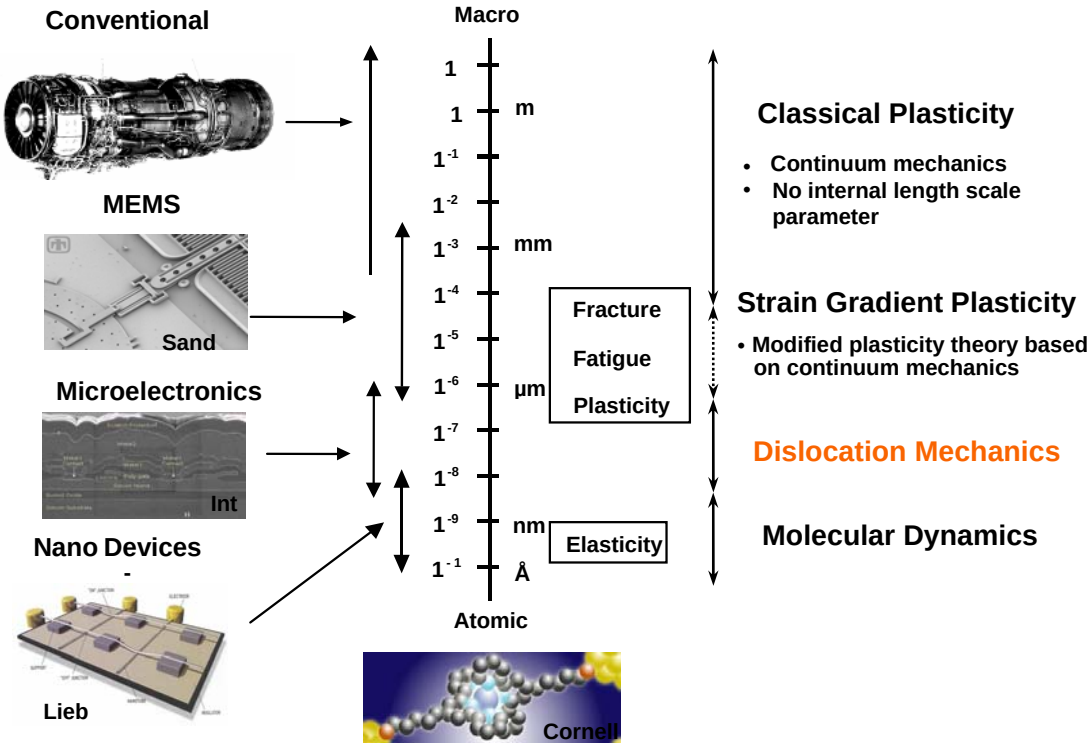

Figure 2.5 Illustration of length-scale effects on the mechanical properties

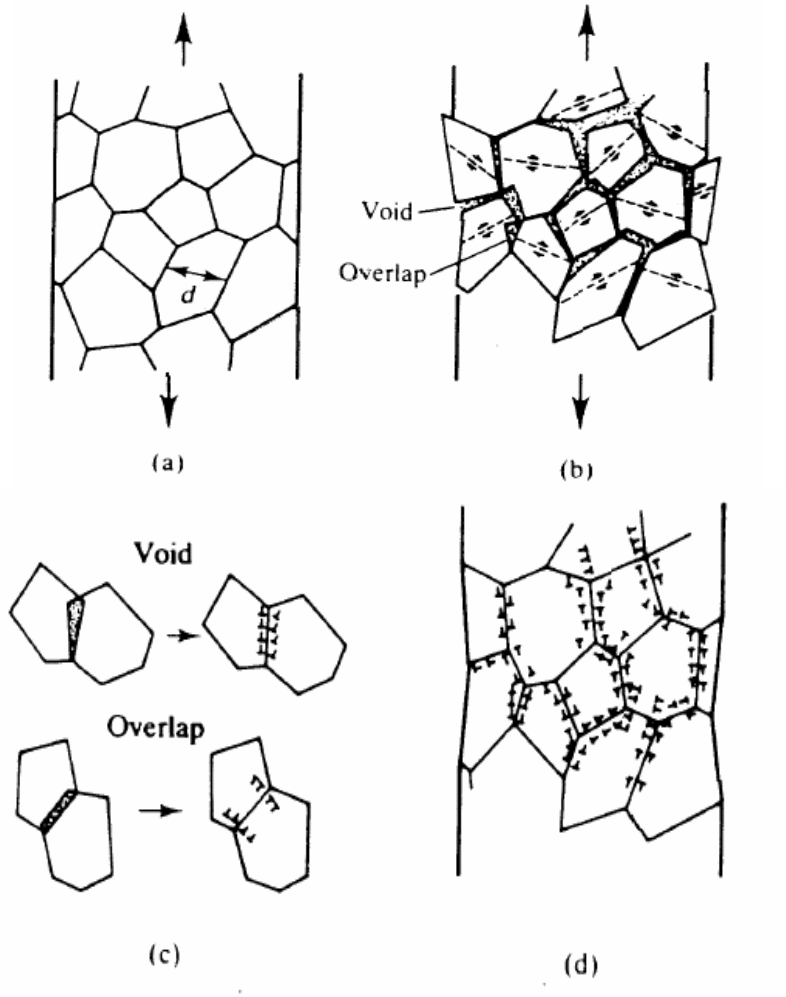

Figure 2.6 Ashby model showing the polycrystal deformation. (a). deforms in a uniform manner; (b) overlaps and voids appear; (c) (d). The voids and overlaps can be corrected by introducing geometrically-necessary dislocations [29].

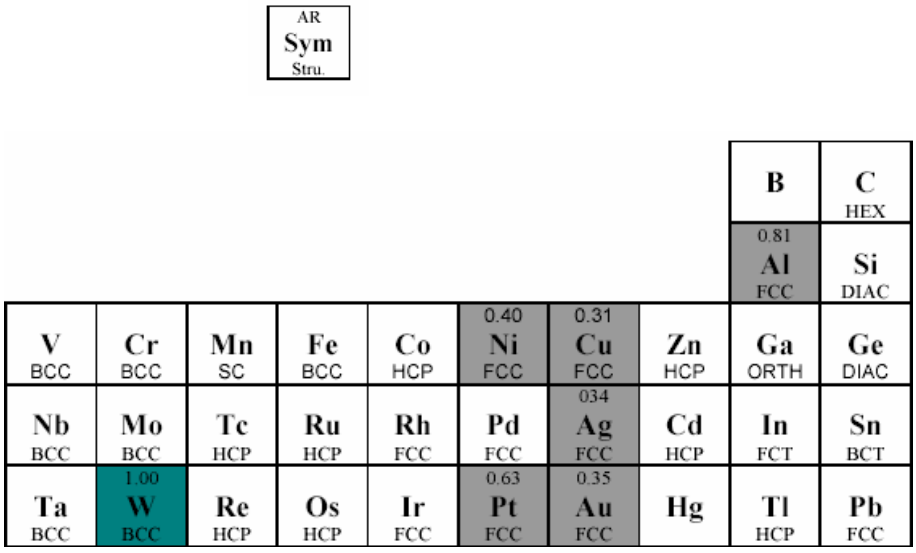

Figure 2.7 Portion of the periodic table showing the FCC metals to be studied (light shading). The number at the top of the box is the anisotropy ratio and the bottom is the structure of the materials.

Table 2.1 Anisotropy Ratio, Stacking Fault Energy and Elastic Modulus for some FCC Materials [31]

Metal	$E_{[100]}$ ***(GPa)***	$E_{[110]}$ ***(GPa)***	$E_{[111]}$ ***(GPa)***	E_{poly} ***(GPa)***	***Anisotropic ratio***	***SFE*** (mJ/m^2)
Al	64	73	76	70	0.81	~250
Pt	136	185	210	170	0.63	~
Ni	137	233	304	200	0.40	~200
Au	43	82	117	78	0.35	~75
Ag	44	84	120	83	0.34	~25
Cu	67	130	190	130	0.31	~90
W	403	403	403	411	1.00	<10

CHAPTER 3

DESIGNS & SIMULATIONS

3.1 Specimen Design

Inspired by the conventional tensile testing bar, the specimen geometry utilized in this study resembles a typical dog-bone specimen but with an area of additional width in the center designed as the contact area where the line load can be applied [28]. This is desired to minimize stress concentrations at the place where the loading device contacts the membrane. The suspended membranes are fixed to the wafer at either end such that they span the bottom view window. In the areas where the membrane is attached to the wafer and in the central contact area the width is varied in such a fashion to minimize boundary bending effects. These effects can also be minimized through large specimen gauge lengths. Thus, a load applied in the center of the span results in direct stretching of the membranes in the areas with thin constant width in the same manner as in a direct tension test.

Specimens with different types and sizes of membranes were designed on a single wafer. Figure 3.1 is a schematic drawing indicating parameters of the membrane dimensions. Actual values are listed in Table 4.2 in the next chapter.

3.2 Thin Film Deposition and Microstructure Modulation

3.2.1 Thin Film Deposition for MEMS

Thin film deposition for MEMS applications can be classified into two groups: depositions that happen because of a chemical reaction and depositions that happen because of a physical reaction. Depositions that happen because of a chemical reaction consist of Electrodeposition, Thermal oxidation, and Chemical Vapor Deposition (CVD), which includes Low Pressure Chemical Vapor Deposition (LPCVD), Atmospheric Pressure Chemical Vapor Deposition (LPCVD), Plasma Enhanced Chemical Vapor Deposition (PECVD), Metal-organic Chemical Vapor Deposition (MOCVD), et al. These processes involve the creation of solid materials directly from chemical reactions in gas and/or liquid compositions or with the substrate material. The solid material is usually not the only product formed by the reaction. Byproducts can include gases, liquids and even other solids. Depositions that happen because of a physical reaction include Casting and Physical Vapor Deposition (PVD), which includes Thermal Evaporation, E-beam Evaporation, Pulsed Laser Deposition (PLD), and Sputtering, et al. Common for all these processes are that the material deposited is physically moved onto the substrate. In other words, it involves physical techniques to form the material on the substrate. This is not completely correct for casting processes, though it is more convenient to think of them in that way.

PVD comprises the standard technologies for deposition of metal thin films. For metals, PVD is far more common than CVD since it can be performed at lower process risk and cheaper considering materials cost. The choice of deposition method (i.e.

evaporation vs. sputtering) may in many cases be arbitrary, and may depend more on what technology is available for the specific material at the time.

In evaporation the substrate is placed inside a vacuum chamber, in which a block (source) of the material to be deposited is also located. The source material is then heated to the point where it starts to boil and evaporate. The vacuum is required to allow the molecules to evaporate freely in the chamber, and they subsequently condense on all surfaces. This principle is the same for all the other evaporation technologies, only the method used to the heat (evaporate) the source material differs. There are two popular evaporation technologies, which are E-beam evaporation and thermal evaporation. In E-beam evaporation, an electron beam is aimed at the source material causing local heating and evaporation. In thermal evaporation, a tungsten boat, containing the source material, is heated resistively with a high current to make the material evaporate. Many materials are restrictive in terms of what evaporation method can be used (i.e. aluminum is quite difficult to evaporate using resistive heating), which typically is related to the phase transition properties of that material. A schematic diagram of a typical E-beam evaporation system is shown in the Figure 3.2 [32].

Sputtering is a technology in which the material is released from the source at much lower temperature than evaporation. The substrate is placed in a vacuum chamber with the source material, named a target, and an inert gas (such as argon) is introduced at low pressure. Gas plasma is created using an RF power source, which causes the gas to become ionized. The ions are accelerated towards the surface of the target, causing atoms of the source material to break off from the target in vapor form and condense on substrate surface. Compared with evaporation, the basic principle of sputtering is the

same for all sputtering technologies. The differences typically relate to the manor in which the ion bombardment of the target is realized. A schematic diagram of a typical RF sputtering system is shown in the Figure 3.3 [33].

3.2.2 Microstructure Modulation

The microstructure of thin films strongly depends on the deposition process involved. Characteristics such as grain size and its distribution, crystallographic orientation and the film density are all affected by the conditions of the process under which grain nucleation, growth, coarsening, coalescence, and thickening occur [34]. Two processing techniques are commonly used to modulate the microstructure of the thin film metal specimens proposed: E-beam evaporation and sputtering. These processes have parameters that cause microstructures to vary. Figure 3.4 is a schematic drawing to illustrate the microstructure modulation in (a) E-Beam evaporation process and (b) sputtering by varying the deposition parameters. Heat treatments of as deposited films can also be used to modulate microstructure. The specimens for heat treatment can be deposited at room temperature and then given systematic heat treatment at modest temperatures and times to develop different microstructures.

3.3 Microscale Plasticity and Fracture Experiments

Plasticity and fracture experiments will be performed on the freestanding thin film membranes using the microscale membrane deflection experiment (MDE) technique developed by Espinosa and Prorok [15-17, 35, 36]. The membrane deflection experiment set-up consists of a nanoindenter to apply line load to the center of the membrane from

the top, and a Mirau microscope interferometer positioned directly below the specimen to independently measure deflection through the microfabricated die window, as shown in Figure 3.5.

3.3.1 Conversion from Nanoindenter Vertical Load to Cauchy Stress

The load data directly obtained from the nanoindenter must be reduced to the load in the plane of membrane, which is found as a component of the vertical nanoindenter load by the following equations:

$$\tan\theta = \frac{\Delta}{L_m} \text{ and } P_M = \frac{P_V}{2Sin\theta}$$

Where (from Figure 3.6) θ is the angle of rotation, Δ is the displacement, L_M is the membrane half-length, P_M is the load in the plane of the membrane, and P_V is the load measured by the nanoindenter. All the parameters are shown in the figure. Once P_M is obtained, the stress, σ(t), can be computed from:

$$\sigma(t) = \frac{P_M}{A}$$

where A is the cross-sectional area of the membrane in the gauge region. Stress-Strain curves then can be generated based on these information provided.

3.3.2 Relationship between Fringe Distance and Strain

As the membrane is deflected by a nanoindenter, the interferometer, which works based on the Michelson Interferometer principle, records the membrane deflection by resolving surface fringes. The fringes result from phase differences of monochromatic

light while it travels different path-lengths to and from the membrane. This light is recombined with a reference beam of fixed path length. When the path-length of the reflected light is a half of a wavelength, λ/2, which is out of phase with the reference beam, they cancel each other resulting in a dark fringe. A fringe will occur at each λ/2 change in vertical height of the membrane.

Figure 3.7 (a) shows a typical monochromatic image obtained and the corresponding relationship between deflections and the distance between fringes. The distance between interference fringes, δ, is related to the wavelength, λ, of the monochromatic light used. By finding the average distance between a number of fringes that are in the focal plane of the interferometer, an overall strain, ε(t), for the membrane can be computed from the following relation:

$$\varepsilon(t) = \frac{\sqrt{\delta^2 + (\lambda/2)^2}}{\delta} - 1$$

$$\delta = \frac{\lambda}{2\tan\theta_1}$$

The above equation is only valid when deflections and angles are small. However, for larger angles a more comprehensive relation is required to account for the additional path length due to reflection off of the deflected membrane. This circumstance is examined in more detail in Fig 3.7 (b). The schematic shows the pathways of the monochromatic light that generate two fringes next to each other. They originate from the objective plane, that is the exit plane of the Mirau objective lens, and then travel to and

reflect off of the deflected membrane to finally return to the objective plane and recombine with the reference beam.

The objective plane also represents the plane where the digital image is captured. At large angles the difference in path length, $\eta + \delta \tan\theta_1$, due to the angled reflection becomes significant enough to affect deflection measurements. Calculated by the geometrical relations, a correction factor can be found to accurately relate the distance (measured between two fringes on the objective plane), with the associated distance between fringes at the membrane plane,

$$\delta \tan\theta_1 + \eta = \lambda \qquad (3.1)$$

In a triangle, using a formula $a^2 + b^2 - 2ab\cos C = c^2$

Thus, $\eta^2 = \delta'^2 + d'^2 - 2\delta' d' \cos\theta_1 \qquad (3.2)$

$$\frac{\delta}{d'} = \cos\theta_1 \Rightarrow d' = \frac{\delta}{\cos\theta_1} \qquad (3.3)$$

Insert Equation 3.3 into 3.2, we get

$$\eta^2 = \delta'^2 + \frac{\delta^2}{\cos^2\theta_1} - 2\delta'\delta \qquad (3.4)$$

Then insert Equation 3.4 into 3.1,

$$\delta \tan\theta_1 + \sqrt{\delta'^2 + \frac{\delta^2}{\cos^2\theta_1} - 2\delta'\delta} = \lambda \qquad (3.5)$$

For δ', from figure 3.7, we have $\delta' = \delta + AB$ (where $AB = \delta \tan\theta_1 \times \tan 2\theta_1$)

Thus, $\delta' = \delta + \delta \tan\theta_1 \tan 2\theta_1 \Rightarrow \delta = \frac{\delta'}{1 + \tan\theta_1 \tan 2\theta_1} \qquad (3.6)$

Plug Equation 3.6 into 3.5,

$$\delta \tan\theta_1 + \sqrt{\delta^2(1+\tan\theta_1 \tan 2\theta_1)^2 + \frac{\delta^2}{\cos^2\theta_1} - 2\delta^2(1+\tan\theta_1 \tan 2\theta_1)} = \lambda \qquad (3.7)$$

$$\left[\delta^2(1+\tan\theta_1 \tan 2\theta_1)^2 + \frac{\delta^2}{\cos^2\theta_1} - 2\delta^2(1+\tan\theta_1 \tan 2\theta_1)\right]^{\frac{1}{2}} = \lambda - \delta\tan\theta_1$$

$$\delta^2(1+\tan\theta_1 \tan 2\theta_1)^2 + \frac{\delta^2}{\cos^2\theta_1} - 2\delta^2(1+\tan\theta_1 \tan 2\theta_1) = \lambda^2 + \delta^2\tan^2\theta_1 - 2\lambda\tan\theta_1\delta$$

$$\delta^2(1+\tan^2\theta_1 \tan^2 2\theta_1 + 2\tan\theta_1 \tan 2\theta_1) + \frac{\delta^2}{\cos^2\theta_1} - 2\delta^2 - 2\delta^2\tan\theta_1 \tan 2\theta_1$$
$$= \lambda^2 + \delta^2\tan^2\theta_1 - 2\lambda\tan\theta_1\delta$$

$$\delta^2(1+\tan^2\theta_1 \tan^2 2\theta_1) + \frac{\delta^2}{\cos^2\theta_1} - 2\delta^2 = \lambda^2 + \delta^2\tan^2\theta_1 - 2\lambda\tan\theta_1\delta$$

$$\delta^2(-1+\tan^2\theta_1 \tan^2 2\theta_1 - \tan^2\theta_1 + \frac{1}{\cos^2\theta_1}) + 2\lambda\tan\theta_1\delta - \lambda^2 = 0 \qquad (3.8)$$

$$-1+\tan^2\theta_1 \tan^2 2\theta_1 - \tan^2\theta_1 + \frac{1}{\cos^2\theta_1}$$
$$= -1+\tan^2\theta_1 \tan^2 2\theta_1 + \frac{1-\sin^2\theta_1}{\cos^2\theta_1}$$
$$= \tan^2\theta_1 \tan^2 2\theta_1$$

Therefore, Equation 3.8 can be rewritten as

$$\delta^2\tan^2\theta_1 \tan^2 2\theta_1 + 2\lambda\tan\theta_1\delta - \lambda^2 = 0 \qquad (3.9)$$

Solve this, we get

$$\delta = \frac{-2\lambda\tan\theta_1 \pm \sqrt{\Delta}}{2\tan^2\theta_1 \tan^2 2\theta_1} \qquad (3.10)$$

Where $\Delta = 4\lambda^2\tan^2\theta_1 - 4\tan^2\theta_1 \tan^2 2\theta_1(-\lambda^2)$

$$= 4\lambda^2 \tan^2\theta_1(1+\tan^2 2\theta_1)$$
$$= \frac{4\lambda^2 \tan^2\theta_1}{\cos^2 2\theta_1} \qquad (3.11)$$

Thus,

$$\delta = \frac{-2\lambda\tan\theta_1 + \frac{2\lambda\tan\theta_1}{\cos 2\theta_1}}{2\tan^2\theta_1 \tan^2 2\theta_1}$$
$$= \frac{\lambda\tan\theta_1(1-\cos 2\theta_1)}{\tan^2\theta_1 \tan^2 2\theta_1 \cos 2\theta_1}$$

$$= \frac{\lambda(2\sin^2\theta)}{\tan\theta_1 \tan 2\theta_1 \sin 2\theta_1}$$
$$= \frac{\lambda}{\tan 2\theta_1}$$

Therefore,

$$\delta = \frac{\lambda}{\tan 2\theta_1} \qquad (3.12)$$

$$\Rightarrow \theta_1 = \frac{1}{2}\arctan\frac{\lambda}{\delta} \qquad (3.13)$$

and $\varepsilon(t) = \frac{1}{\cos\theta_1} - 1$

Using Equation 3.13, the finite strain can be expressed as,

$$\varepsilon(t) = \frac{1}{\cos(\frac{1}{2}\arctan\frac{\lambda}{\delta})} - 1 \qquad (3.14)$$

Using these two different strain expressions, we plotted the finite strain versus the deflection angle. As shown in figure 3.9, it shows great agreement when the deflection

angle is less than 3 degrees by comparison of the two expressions. In actual membrane deflection experiment, most membranes will fracture within the deflection angle of 3 degrees.

Thus, the finite strain can be expressed as:

$$\varepsilon(t) = \frac{\sqrt{\delta^2 + (\lambda/2)^2}}{\delta} - 1 \qquad (3.15)$$

3.4 Overestimation of Elastic Modulus

3.4.1 Calculation of the Elastic Modulus for Thin Films

As stated in chapter 3.3, the Stress-Strain curve can be generated based on the Cauchy stress converted from the nanoindenter vertical load and also the strain calculated from distance between interference fringes, δ, which is related to the wavelength, λ. It is noted that the Cauchy stress represented as $\sigma(t) = \frac{P_M}{A}$, where A is the cross-sectional area of the membrane in the gauge region. Actually the specimen resembles a typical dog-bone tensile specimen and is designed in a fashion that width is varied to minimize boundary-bending effects. As a result, the cross section of the specimen is varied due to varied width of the specimen. We take the cross-sectional area of the membrane in the gauge region for simplicity due to the non-linear variation of the width of the specimen. As a result, the actual elastic modulus may be different from the elastic modulus using the methods calculated above.

3.4.2 Effects of Different Window Sizes on Elastic Modulus

Figure 3.1 shows the geometry of the specimen, in which the width of the taped region is designed in a fashion that changes gradually. In order to calculate the elastic modulus, we consider the cross-section area of the taped region the same as the gauge membrane region for convenience. However the extra cross-sectional area in the taped region makes the membrane harder to deform thus the calculated the elastic modulus can be larger than the actual elastic modulus. We are interested in how much difference between the calculated elastic modulus and actual elastic modulus when we simply consider the cross-section area of the gauge region for the cross-section of the whole specimen. In this study, we also change the sizes of bottom view window in a series to see the influence on the calculated elastic modulus of the specimen.

3.4.2.1 Simple Analytical Solution for Overestimation of Elastic Modulus for Specimen

We simply use square-shaped geometry resembles one half of the membrane. This simple geometry avoids the non-linear variation of the width of the taped region and is easier for analytical solution. Figure 3.10 shows the geometrical representation and also the definition of the symbols. The pulling force is applied to mimic the force on the membranes.

Symbol definition:

L_1' length of area 1 after deformation

L_2' length of area 2 after deformation

A_1 cross section area of area 1

A_2 cross section area of area 2

ε strain of total area

ε_1 strain of total area 1

ε_2 strain of total area 2

σ_1 stress of area 1

σ_2 stress of area 2

E elastic modulus of material

E' calculated elastic modulus

From Figure 3.10, we can get

$$\varepsilon_1 = \frac{\sigma_1}{E} = \frac{F}{A_1 \times E} = \frac{F}{W_1 \times T \times E} = \frac{L_1' - L_1}{L_1}$$

$$L_1' = \frac{F \times L_1}{W_1 \times T \times E} + L_1$$

$$\varepsilon_2 = \frac{\sigma_2}{E} = \frac{F}{A_2 \times E} = \frac{F}{W_2 \times T \times E} = \frac{L_2' - L_2}{L_2}$$

$$L_2' = \frac{F \times L_2}{W_2 \times T \times E} + L_2$$

$$\varepsilon = \frac{L_2' + L_1' - (L_2 + L_1)}{L_2 + L_1}$$

$$= \frac{\frac{F \times L_2}{W_2 \times T \times E} + L_2 + \frac{F \times L_1}{W_1 \times T \times E} + L_1 - (L_2 + L_1)}{L_2 + L_1}$$

$$= \frac{\frac{F \times L_2}{W_2 \times T \times E} + \frac{F \times L_1}{W_1 \times T \times E}}{L_2 + L_1}$$

$$= \frac{F \times L_2 \times W_1 + F \times L_1 \times W_2}{W_2 \times W_1 \times T \times E \times (L_2 + L_1)}$$

Therefore,

$$\varepsilon = \frac{F \times L_2 \times W_1 + F \times L_1 \times W_2}{W_2 \times W_1 \times T \times E \times (L_2 + L_1)} \tag{3.16}$$

Since $E' = \frac{\sigma'}{\varepsilon} = \frac{F}{A_1 \times \varepsilon}$ (3.17)

Insert Equation 3.16 into 3.17,

$$E' = \frac{\sigma'}{\varepsilon} = \frac{F}{A_1 \times \varepsilon} = \frac{F}{A_1 \times \frac{F \times L_2 \times W_1 + F \times L_1 \times W_2}{W_2 \times W_1 \times T \times E \times (L_2 + L_1)}}$$

$$= \frac{F \times W_2 \times W_1 \times T \times E \times (L_2 + L_1)}{W_1 \times T \times (F \times L_2 \times W_1 + F \times L_1 \times W_2)}$$

$$= \frac{W_2 \times E \times (L_2 + L_1)}{L_2 \times W_1 + L_1 \times W_2}$$

$$E' = \frac{E \times (L_2 \times W_1 - L_2 \times W_1 + L_2 \times W_2 + W_2 \times L_1)}{L_2 \times W_1 + L_1 \times W_2}$$
$$= \frac{E \times (L_2 \times W_1 + L_1 \times W_2 + L_2 \times W_2 - L_2 W_1)}{L_2 \times W_1 + L_1 \times W_2}$$
$$= E + E \times \frac{L_2 \times (W_2 - W_1)}{L_2 \times W_1 + L_1 \times W_2}$$

Therefore,

$$E' = E + E \times \frac{L_2 \times (W_2 - W_1)}{L_2 \times W_1 + L_1 \times W_2} \qquad (3.18)$$

E' is the calculated elastic modulus of the specimen and E is the actual elastic modulus. W_2 is greater than W_1 to mimic the actual geometry of the membrane. As a result, the calculated elastic modulus is always greater than the actual elastic modulus of the specimen. From the analytical solution mentioned above, we will overestimate the elastic modulus of the specimen if W_2 is larger than W_1.

3.4.2.2 Overview of Finite Element Analysis and ANSYS Software

Finite element analysis (FEA) was first developed for use in the aerospace and nuclear industries where the safety of structures is critical. Today, the increasing usage of the method is directly attributed to the rapid advances in computer technology in recent years. As a result, commercial finite element packages exist that are capable of solving the most sophisticated problems, not just for structural analysis, but also used in the analysis of a wide range of phenomena such as steady state, dynamic temperature distributions, fluid flow and manufacturing processes such as injection molding and metal forming.FEA consists of a computer model of a material or design that is loaded and analyzed for specific results. It can be used in new product design, and existing product

refinement. Mathematically, the structure to be analyzed is subdivided into a mesh of finite sized elements with simple shapes. Within each element, the variation of displacement is assumed to be determined by simple polynomial shape functions and nodal displacements. Equations for the strains and stresses are developed in terms of the unknown nodal displacements. From that, the equations of equilibrium are assembled in a matrix form which can be easily be programmed and solved on a computer. After applying the appropriate boundary conditions, the nodal displacements are found by solving the matrix stiffness equation. Once the nodal displacements are known, element stresses and strains can be calculated. For each of these modeling schemes, the programmer can insert numerous algorithms (functions) which may make the system behave linearly or non-linearly. Linear systems are far less complex and generally ignore many subtleties of loading and behavior. Non-linear systems can account for more realistic behavior such as plastic deformation, changing loads etc. and is capable of testing a component all the way until failure. Despite the proliferation and power of software packages commercially available, it is essential to have an understanding of the technique and physical processes involved in the analysis. Only then can an analysis model be appropriately selected, correctly defined and subsequently interpreted.

ANSYS is a general purpose finite element modeling package for numerically solving a wide variety of mechanical problems. These problems may include: static/dynamic structural analysis (both linear and non-linear), heat transfer and fluid problems, as well as acoustic and electromagnetic problems. Study of physical responses, such as stress levels, temperature distributions, or the impact of electromagnetic fields as well as optimization of a design is well preformed by ANSYS software.

3.4.2.2 Numerical Simulation of Membranes with Different Window Sizes

In order to get more accurate results than simple analytical solution by using the actual geometry of membranes, numerical simulation by ANSYS software is performed. By ANSYS software, the actual geometry of the membrane is being used in the simulation to see the physical responses of applying load.

The numerical simulation process mimics the membrane deflection test. By applying load at the center of the membrane and calculating the corresponding strain using the simulation, elastic modulus is calculated using the simplified methods. Numerical simulations of 9 membranes in the same group with different bottom view window sizes are preformed. The geometrical dimension of each membrane is listed in Table 3.1. Before the simulation process, element type of the membrane, element real constants, material properties, and the model geometry are defined. The actual elastic modulus of the membrane is input as material properties. The elastic modulus of gold (78GPa) is used in the simulation. Element type can be selected from 150 different element types in the ANSYS element library. In this study, Shell63 model is used to describe the material properties. Shell63 model has both bending and membrane capabilities. Both in-plane and normal loads are permitted. Another series of simulation is performed using Solid45 model. Solid45 model is used for the 3-D modeling of solid structures. The element has plasticity, creep, swelling, stress stiffening, large deflection, and large strain capabilities. Figure 3.11 shows the deformation shapes of 9 specimens under applied load using shell63 model simulation. The different color represents different displacement level of deformation. Figure 3.12 shows the deformation shape showing strain level of the specimens under applied load using solid45 model simulation.

From the numerical simulations, it shows the overestimation of elastic modulus than the real elastic modulus. The elastic modulus and the errors calculated from the simulation results and the equation 3.18 are listed in Table 3.2. And by using solid45 model it gives more estimation of elastic modulus than the shell63 model. Figure 3.13 shows the overestimation of elastic modulus vs. length ratio of the specimen from numerical simulations and simply analytical solution. All of them show the overestimation of elastic modulus. Simulation results show that as the ratio of L_1 to L_2 increases, the error due to the broader edges decreases, which can be explained by our previous equation 3.18.

$$E' = E + E \times \frac{L_2 \times (W_2 - W_1)}{L_2 \times W_1 + L_1 \times W_2}$$

$$E' - E = E \times \frac{L_2 \times (W_2 - W_1)}{L_2 \times W_1 + L_1 \times W_2}$$

$$= \frac{W_2 - W_1}{W_1 + \frac{L_1}{L_2} \times W_2}$$

Therefore, as $\frac{L_1}{L_2}$ increases, E'-E decreases.

The simulation results using the shell63 model show great agreement with the results from the simply analytical solution. The trend has been well explained by figure 3.13.

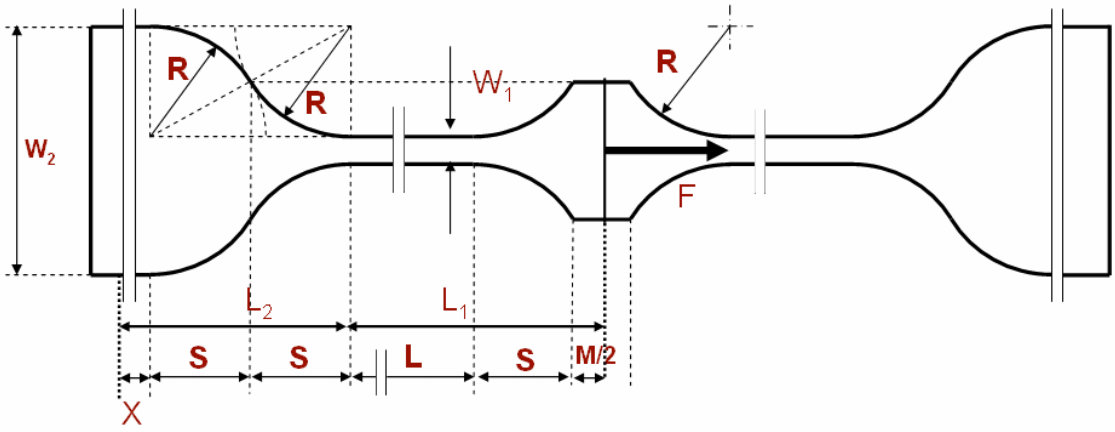

Figure 3.1 Schematic of membrane geometry indicating the different parameters used to define specimen dimensions [36]

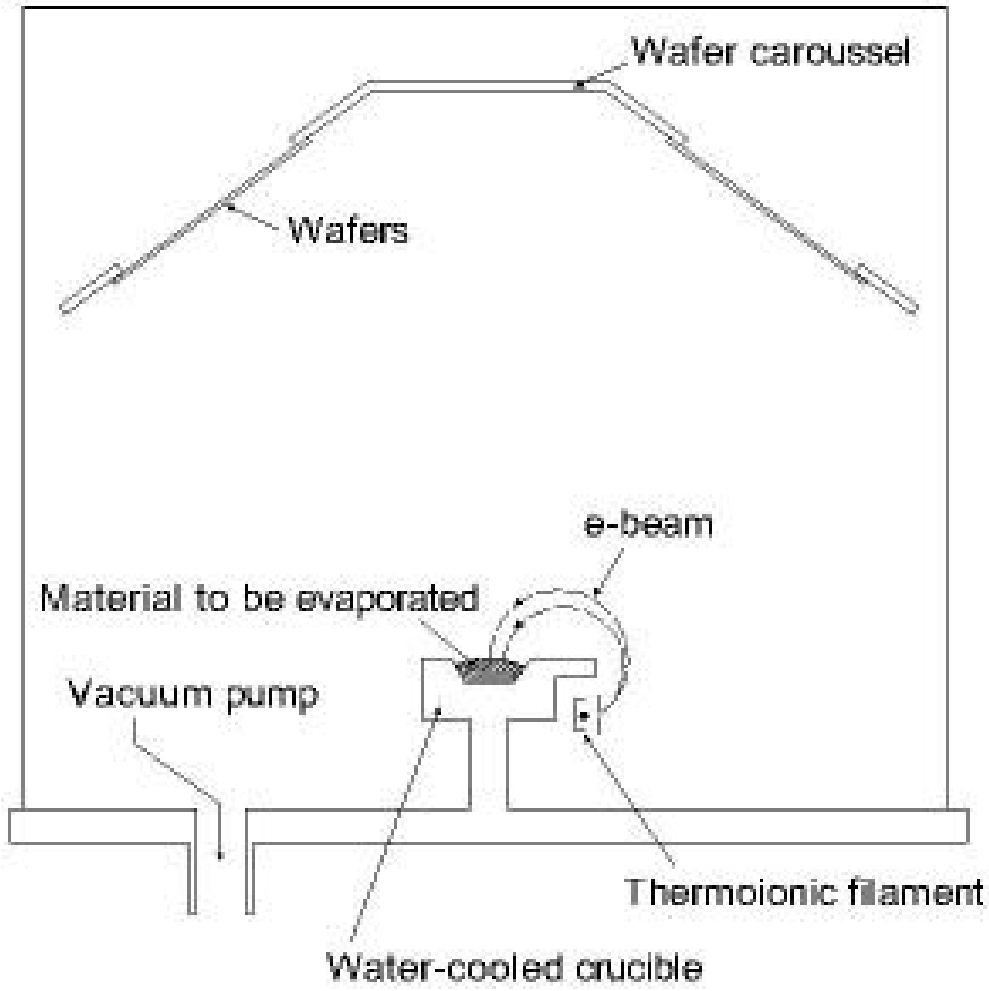

Figure 3.2 A typical system for E-beam evaporation [32]

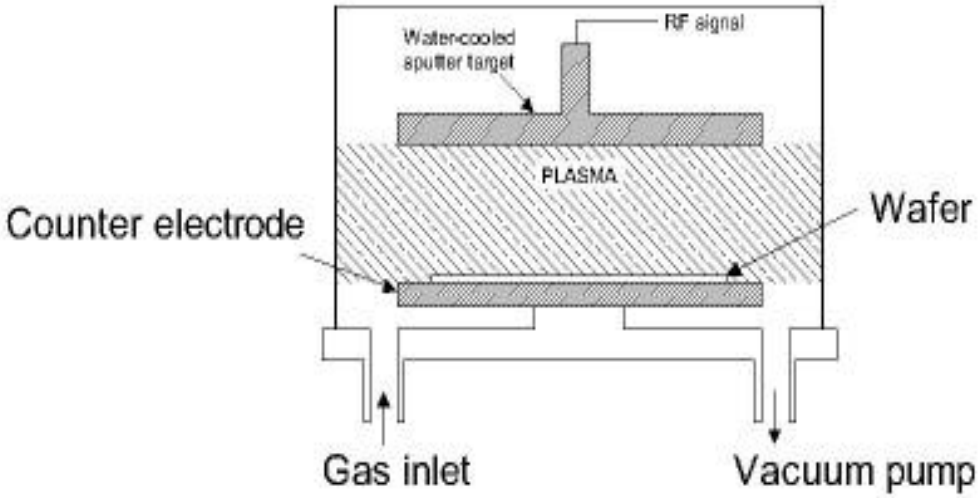

Figure 3.3 A typical RF sputtering system [33]

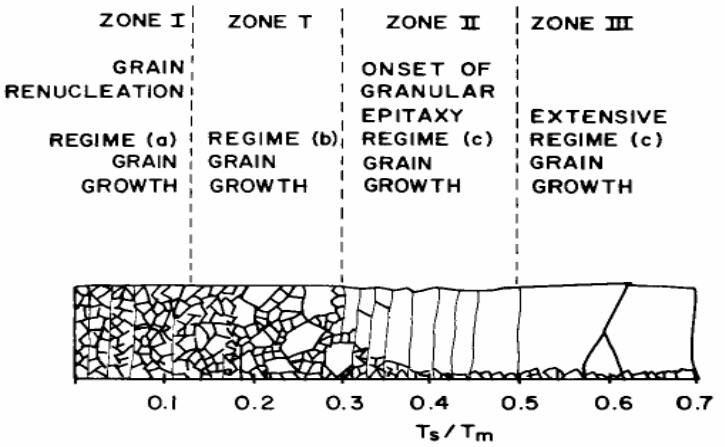

(a)

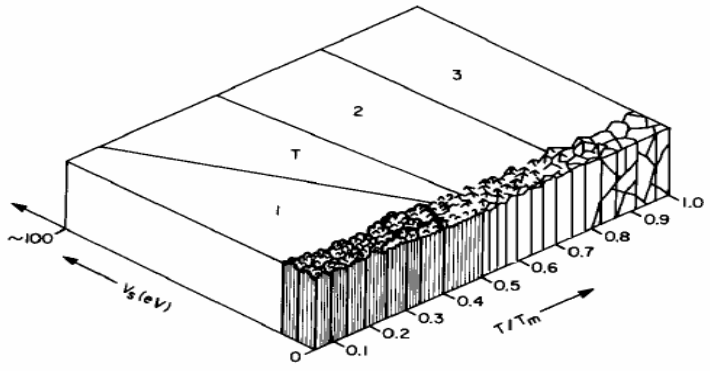

(b)

Figure 3.4 Modulation of microstructure by manipulation of deposition parameters.(a) Substrate temperature effect on the microstructure of evaporated films [37]. (b) Microstructure of RF-sputtered films showing effects of both substrate bias voltage and substrate temperature [38].

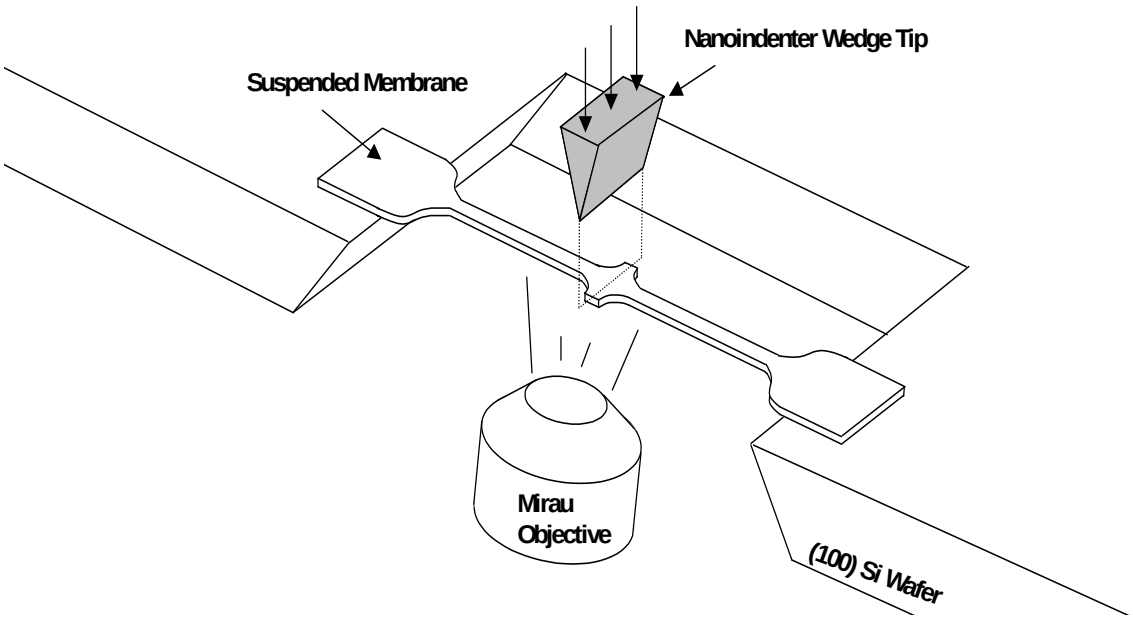

Figure 3.5 3D schematic view of the membrane deflection experiment [39]

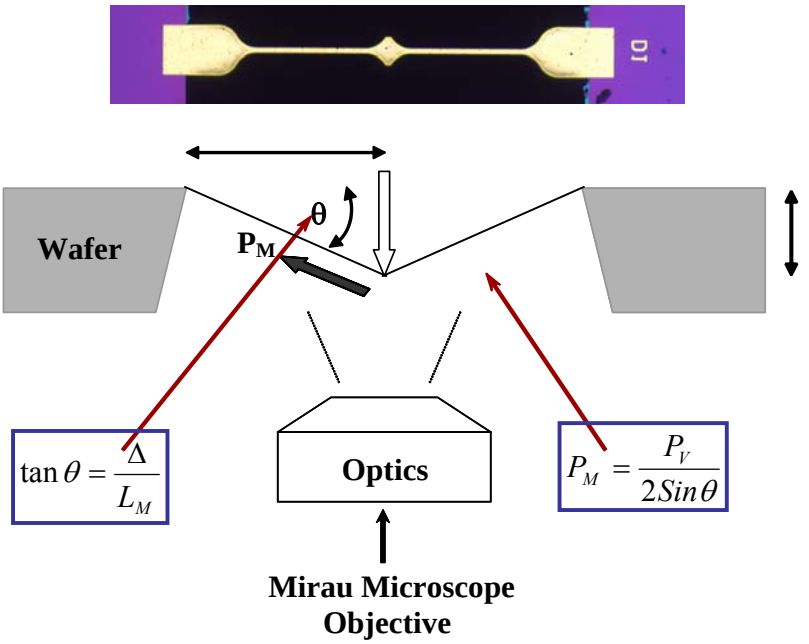

Figure 3.6 Side view of the MDE test showing vertical load being applied by the nanoindenter, P_V, the membrane in plane load, P_M, and the position of the Mirau microscope objective [16].

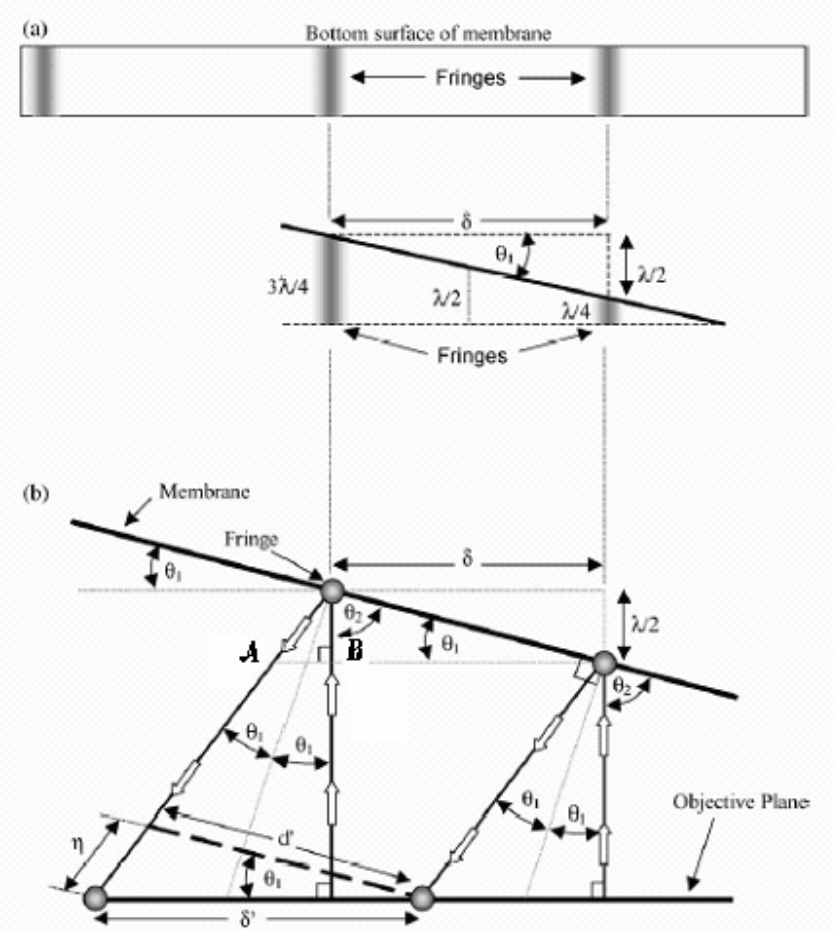

Figure 3.7 Schematic representations showing the relationship between the distances between fringes (δ), wavelength of the monochromatic light used (λ), and vertical displacement (a) and the correction in path length, η, to account for the angled reflection at large values of θ_1(b) [16].

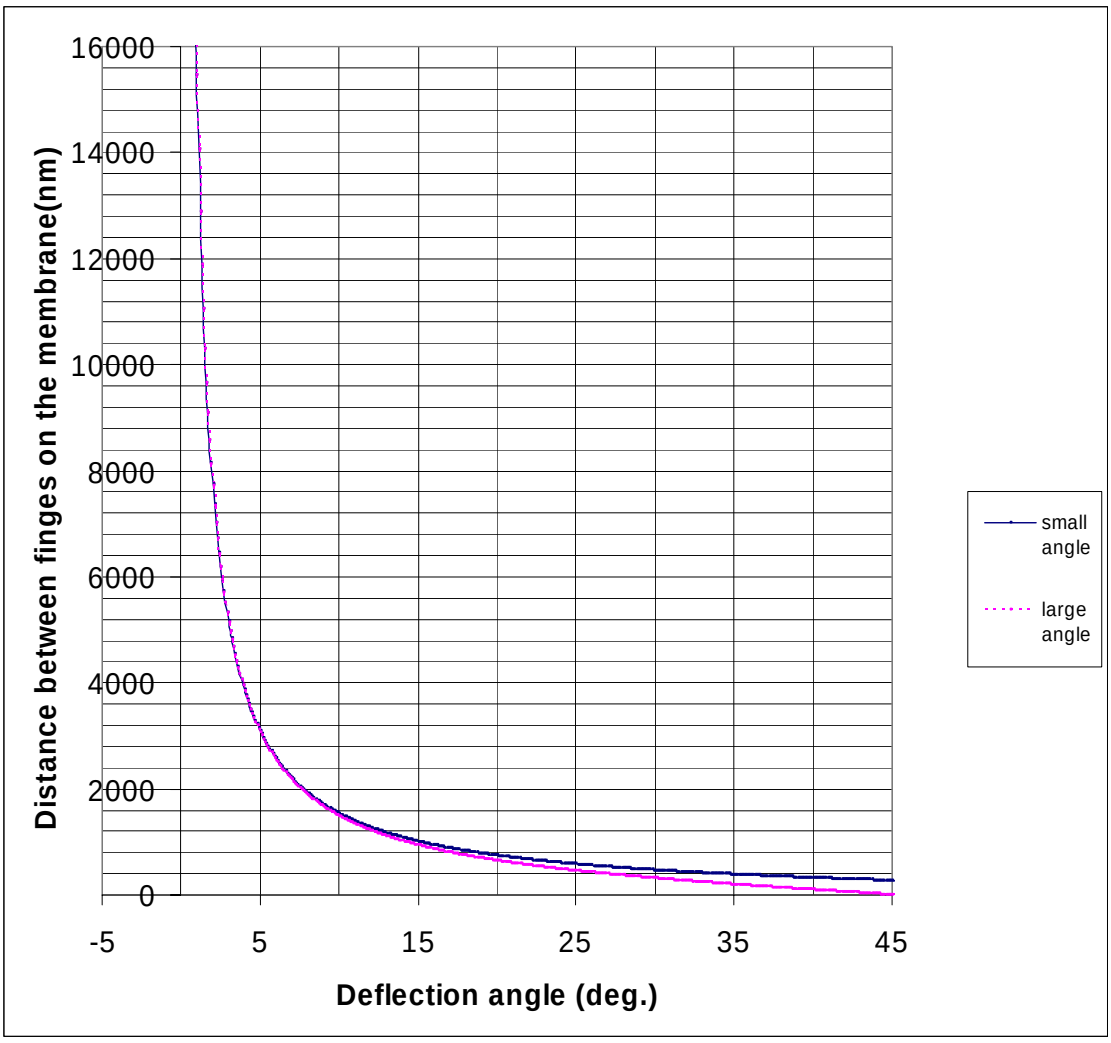

Figure 3.8 Distance between fringes on the membrane versus the deflection angle

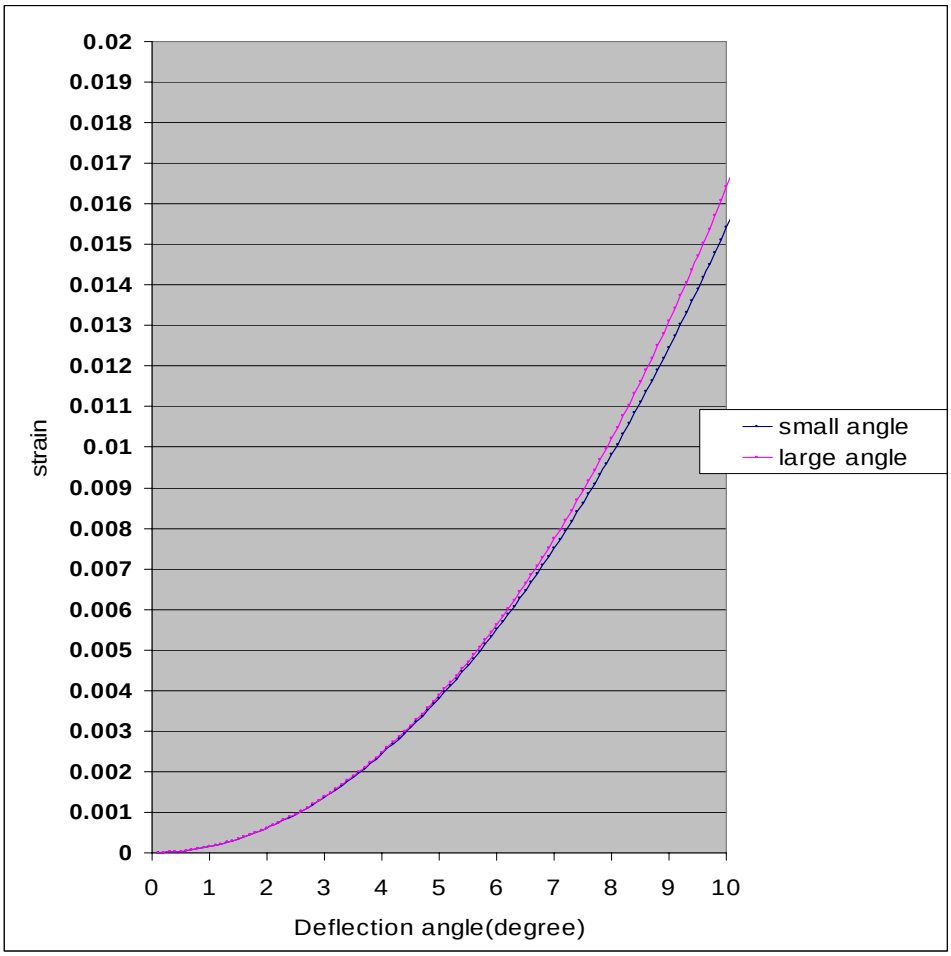

Figure 3.9 Finite strain versus deflection angle using small angle expression and large angle expression.

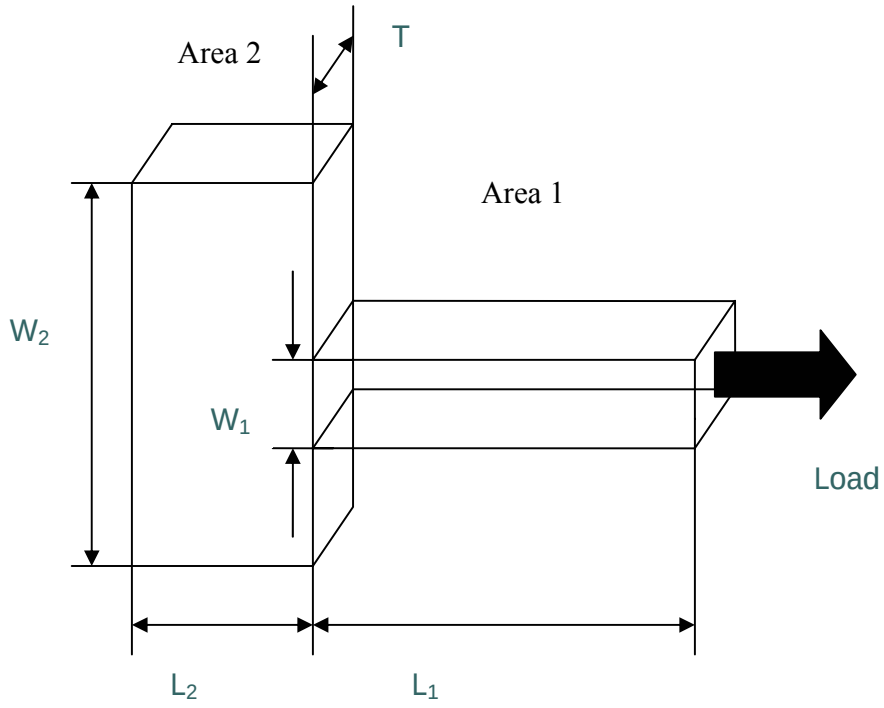

Figure 3.10 Geometrical representation of square-shaped geometry resembles one half of the membrane

Definition of symbols:

L_1, L_2: length of area 1 and area 2

W_1, W_2: width of area 1 and area 2

T: thickness

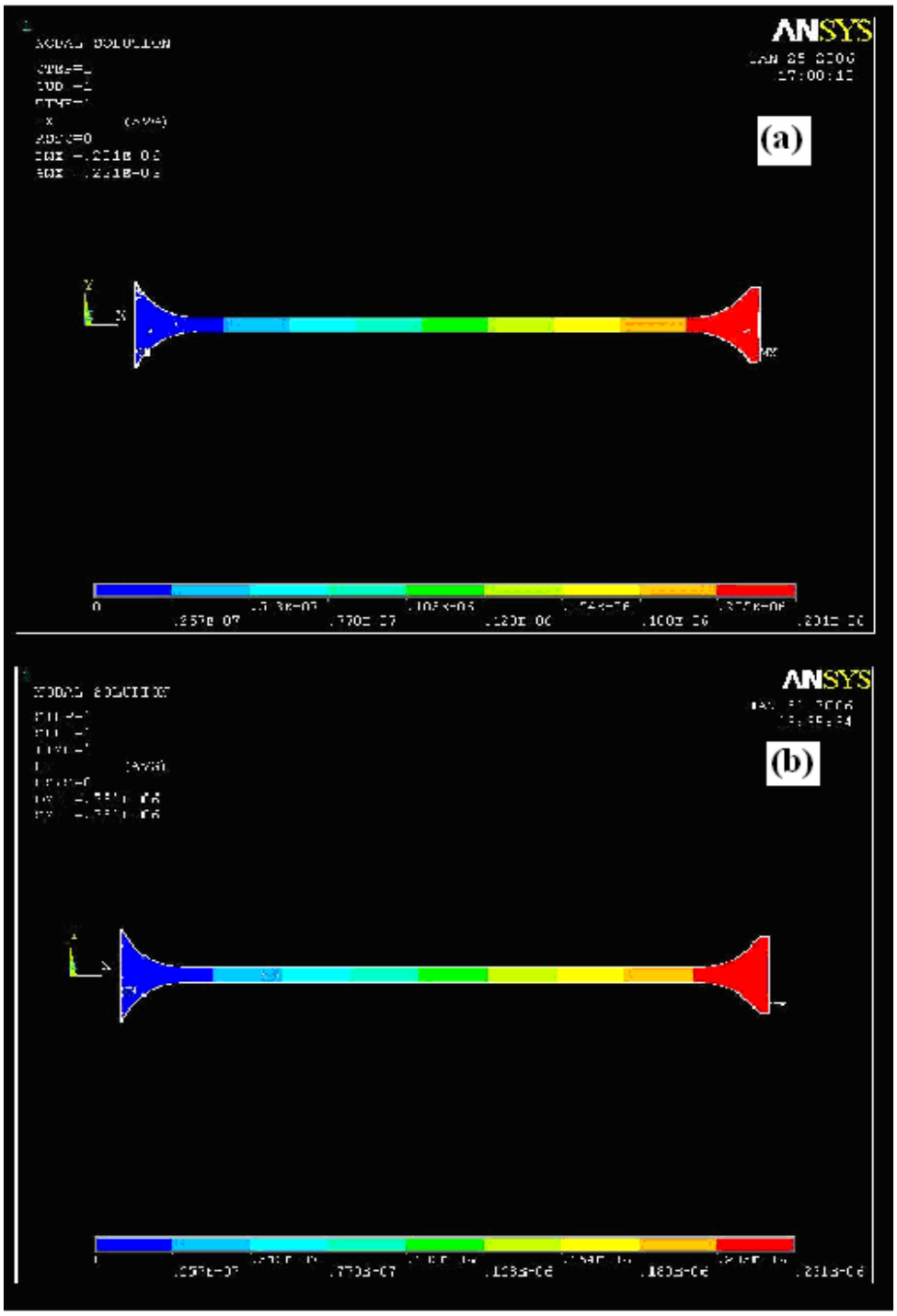

Figure 3.11 Deformation shapes of 9 specimens under applied load using shell63 model simulation (a) & (b)

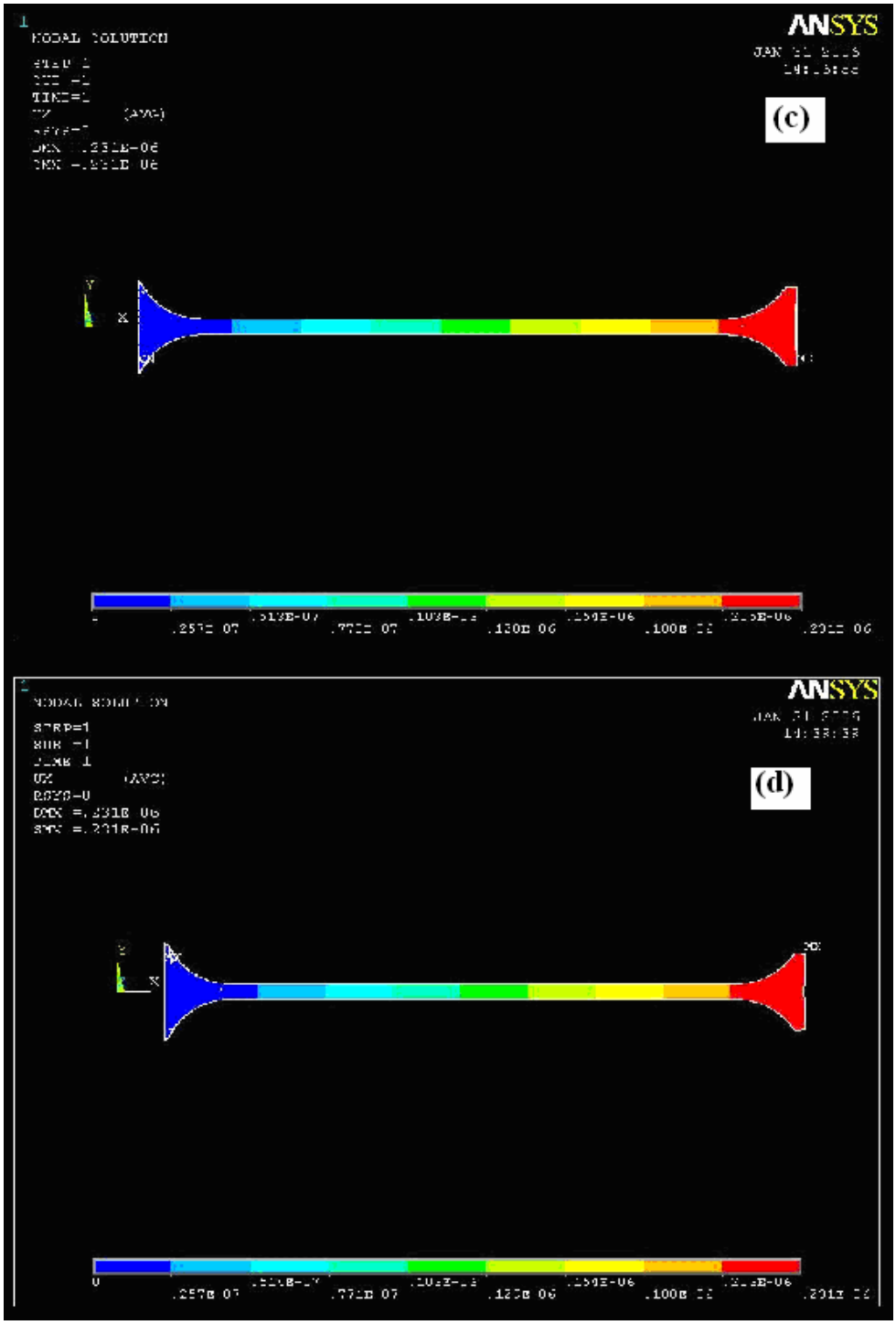

Figure 3.11 Deformation shapes of 9 specimens under applied load using shell63 model simulation (c) & (d)

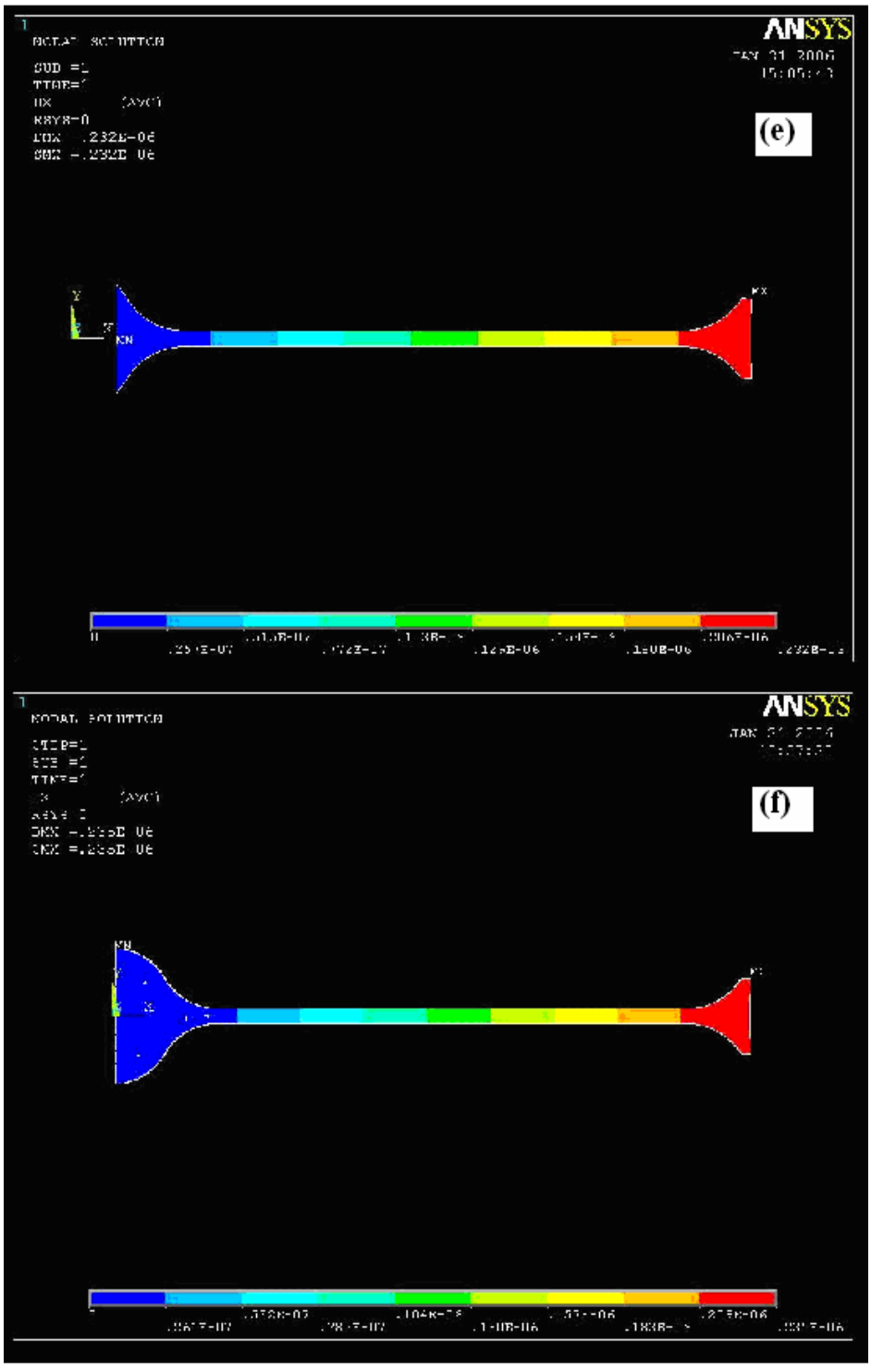

Figure 3.11 Deformation shapes of 9 specimens under applied load using shell63 model simulation (e) & (f)

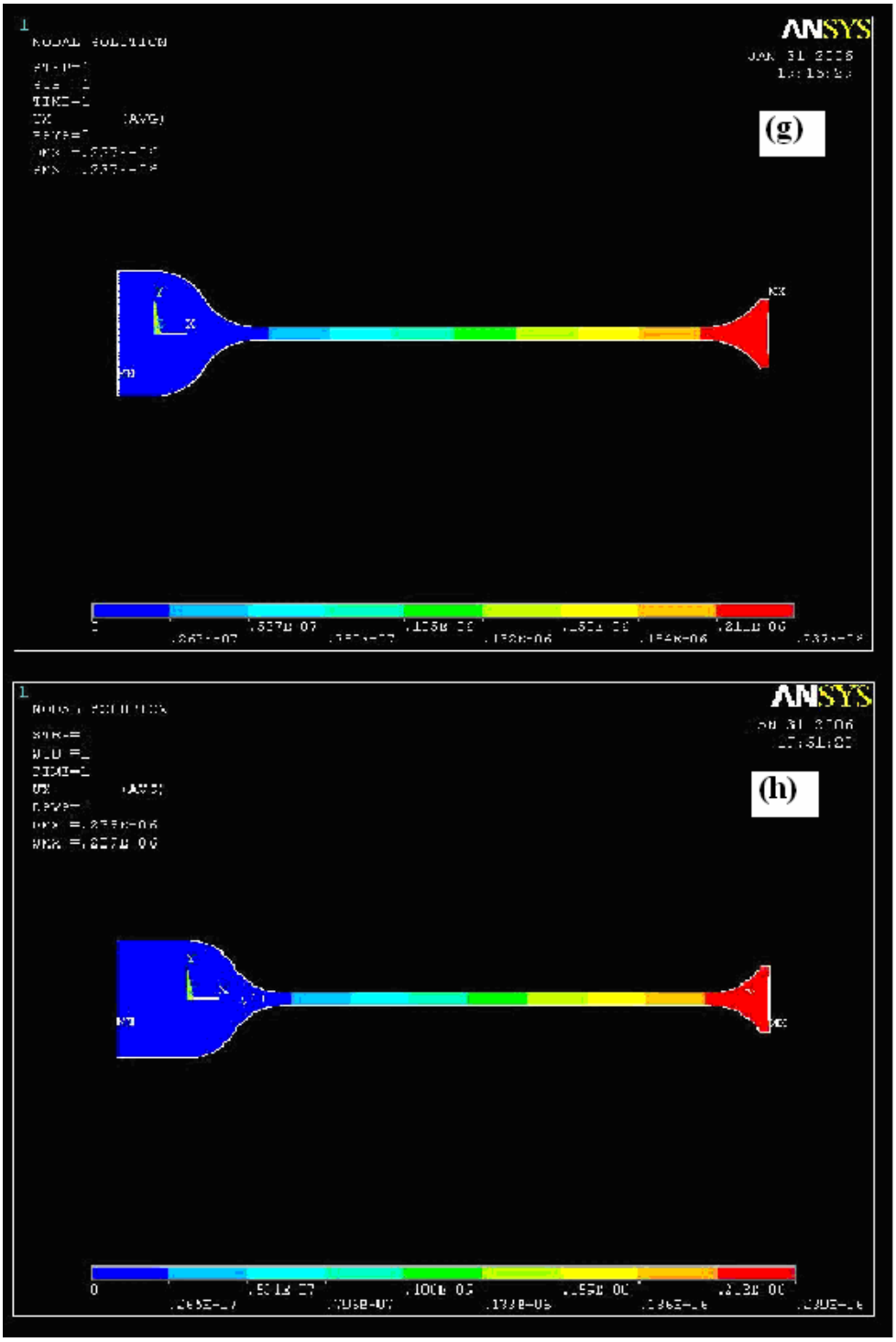

Figure 3.11 Deformation shapes of 9 specimens under applied load using shell63 model simulation (g) & (h)

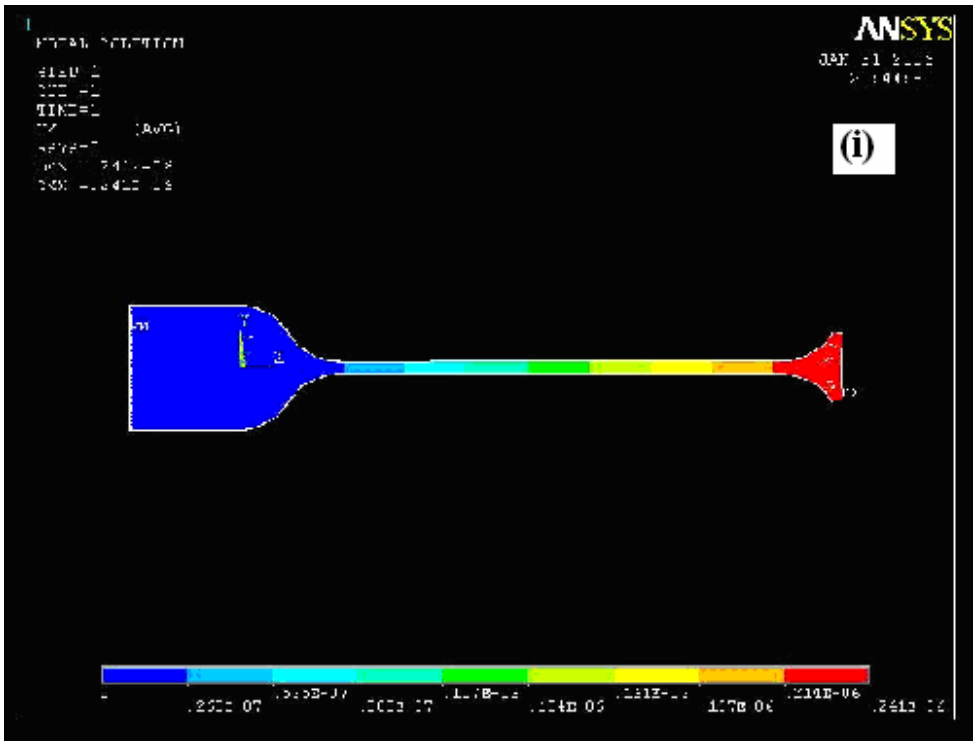

Figure 3.11 Deformation shapes of 9 specimens under applied load using shell63 model simulation (i)

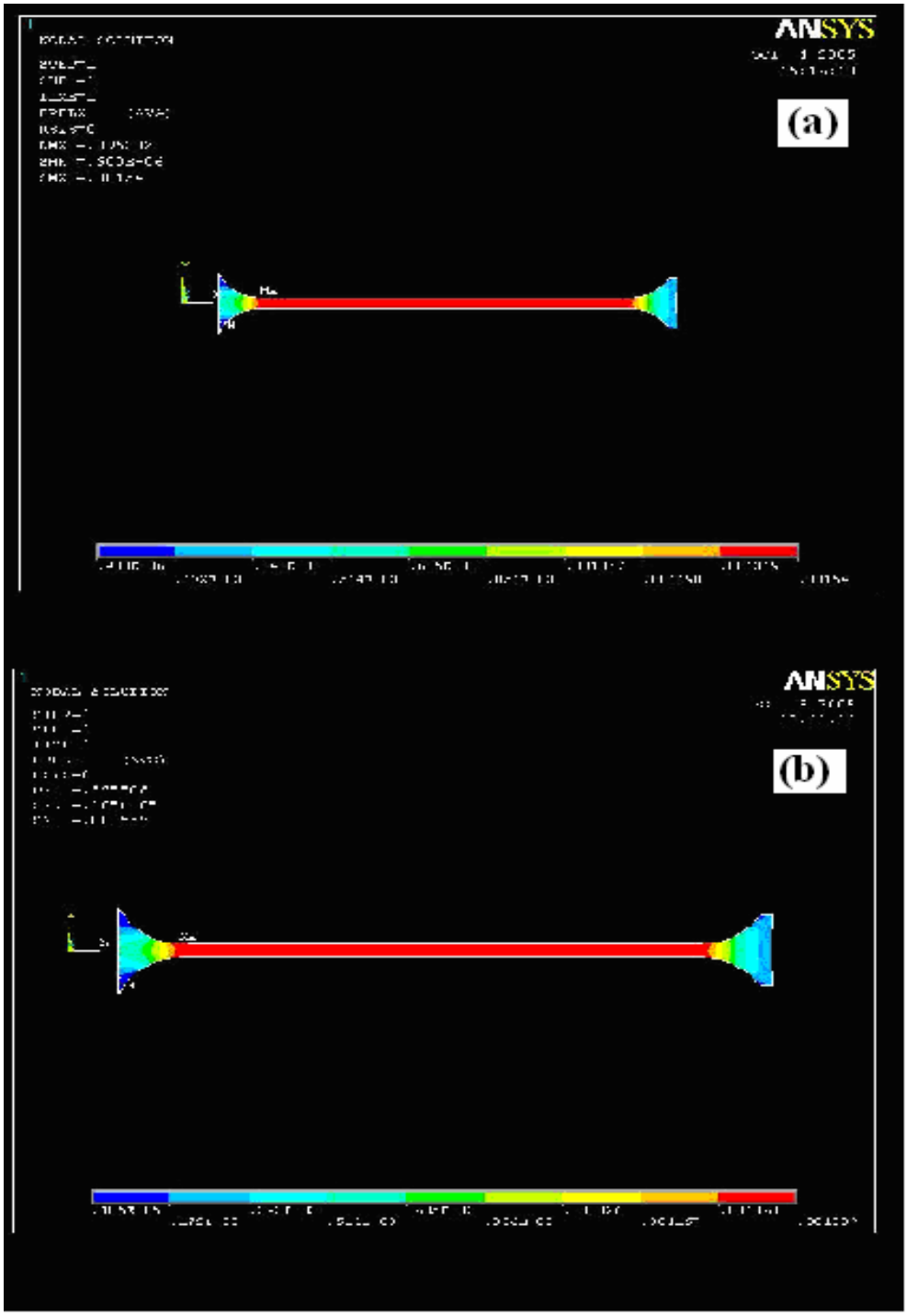

Figure 3.12 Deformation shapes of 9 specimens under applied load using Solid45 model simulation (a) & (b)

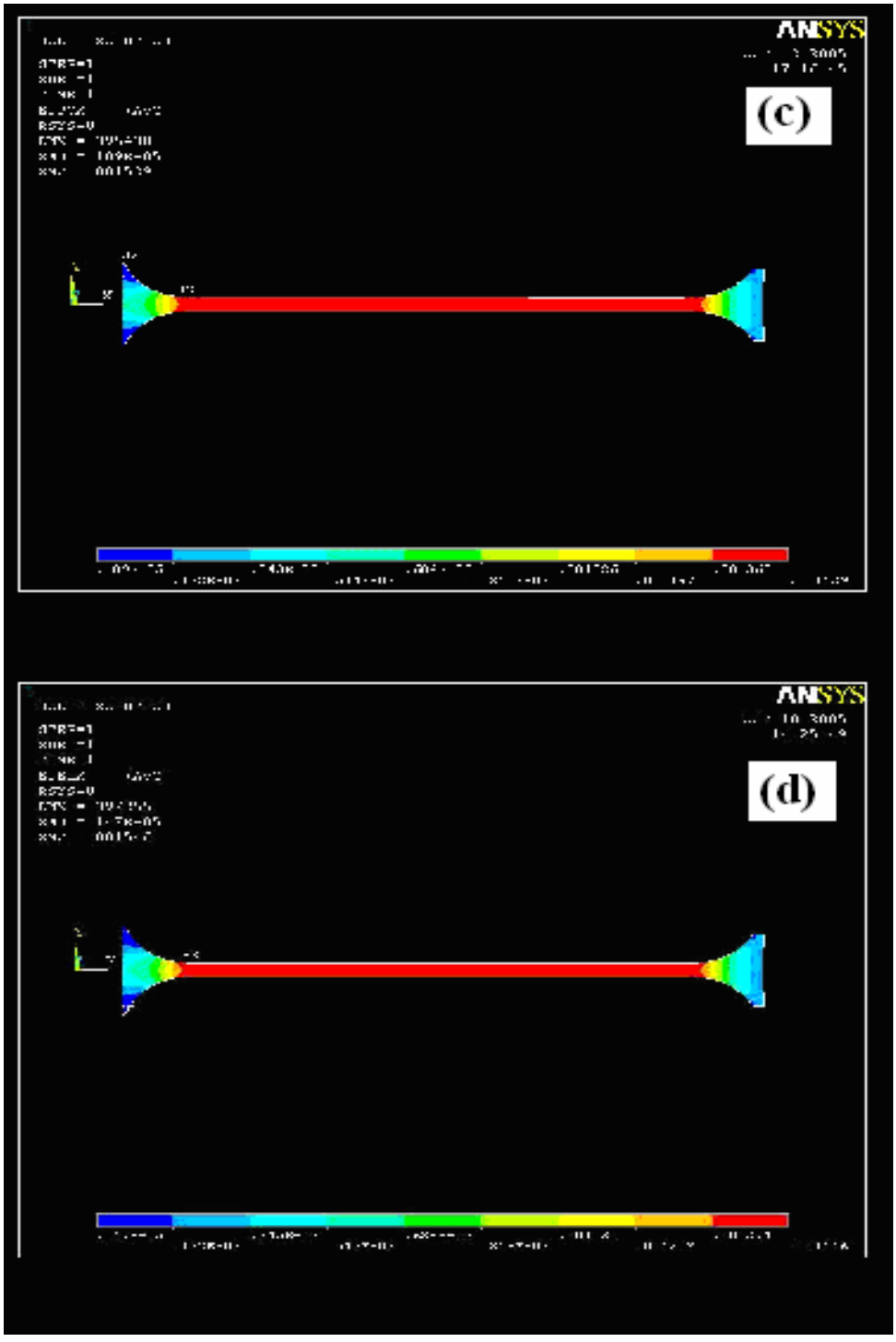

Figure 3.12 Deformation shapes of 9 specimens under applied load using Solid45 model simulation (c) & (d)

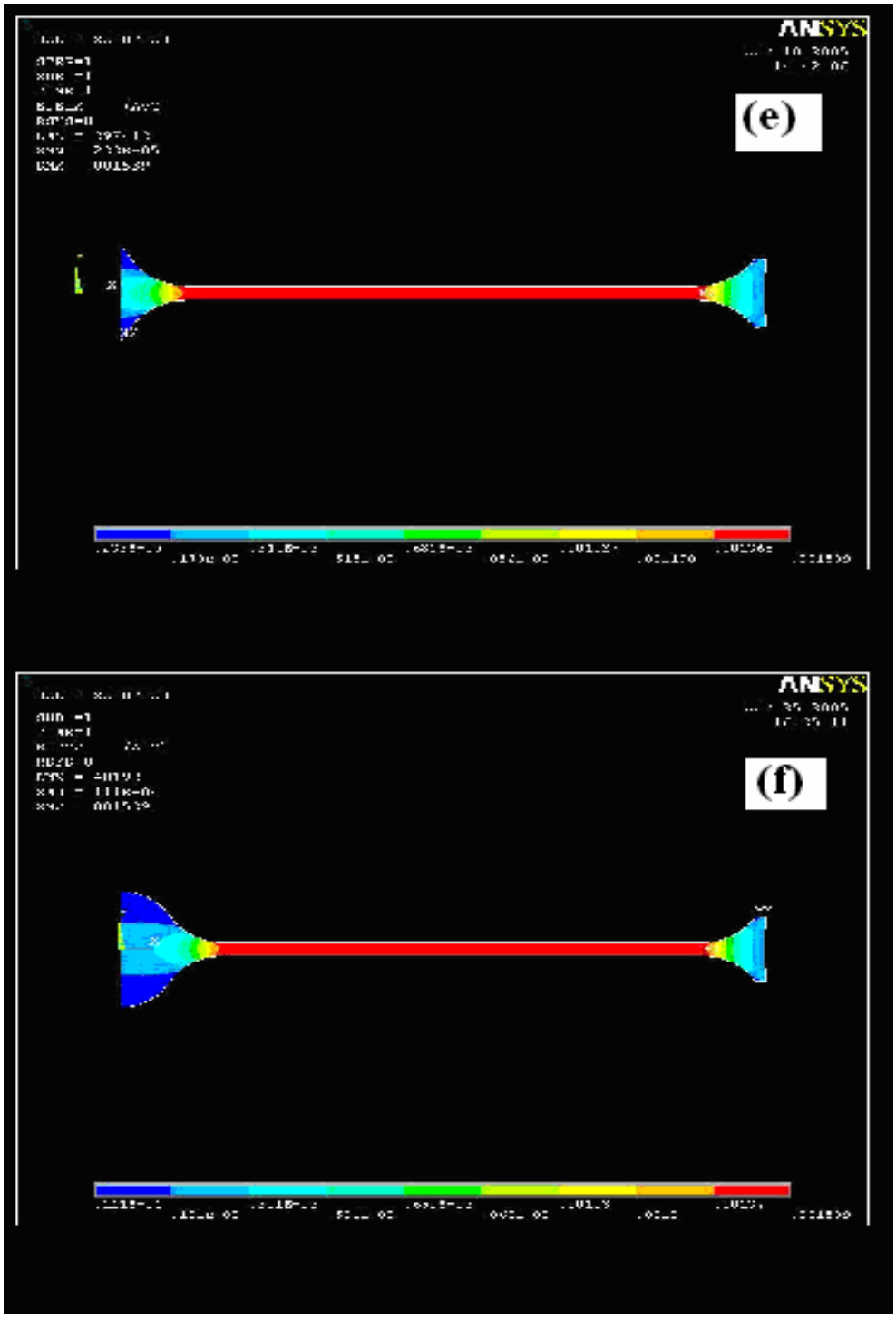

Figure 3.12 Deformation shapes of 9 specimens under applied load using Solid45 model simulation (e) & (f)

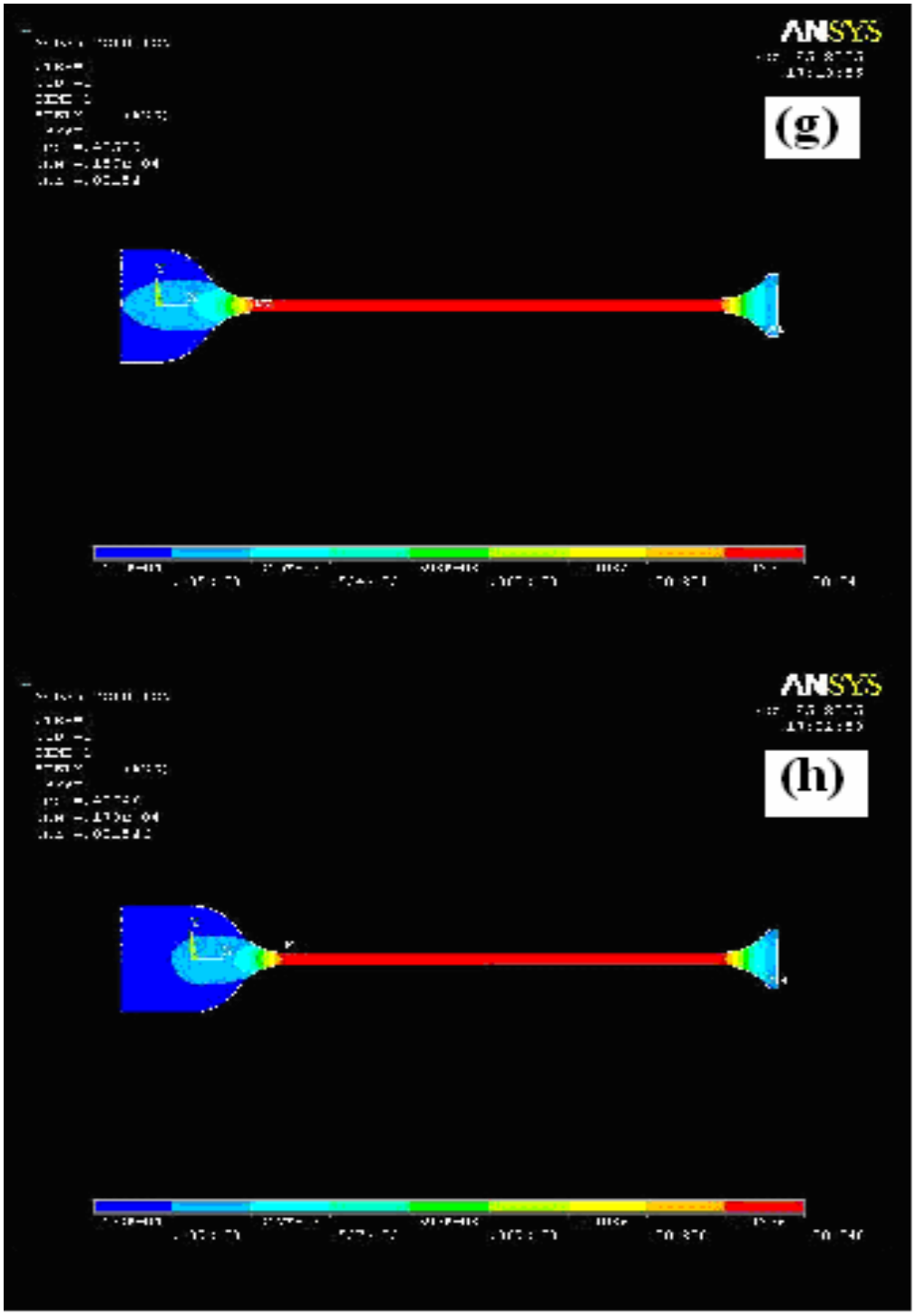

Figure 3.12 Deformation shapes of 9 specimens under applied load using Solid45 model simulation (g) & (h)

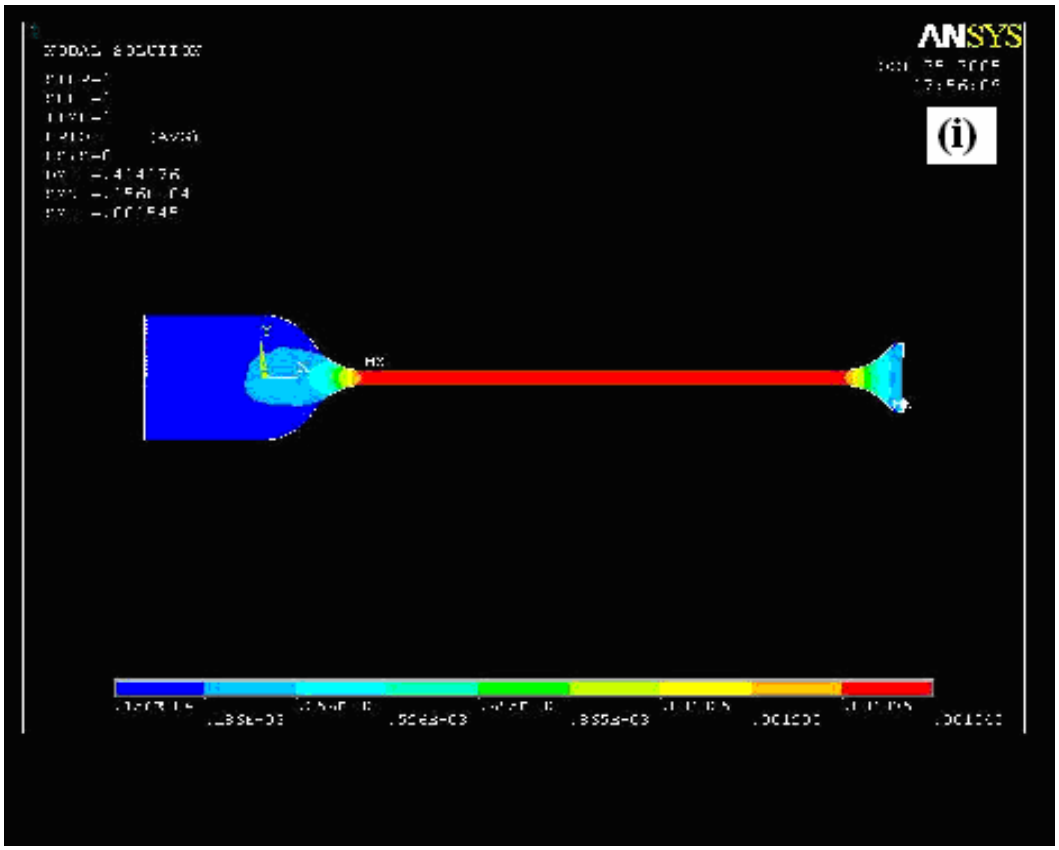

Figure 3.12 Deformation shapes of 9 specimens under applied load using Solid45 model simulation (i)

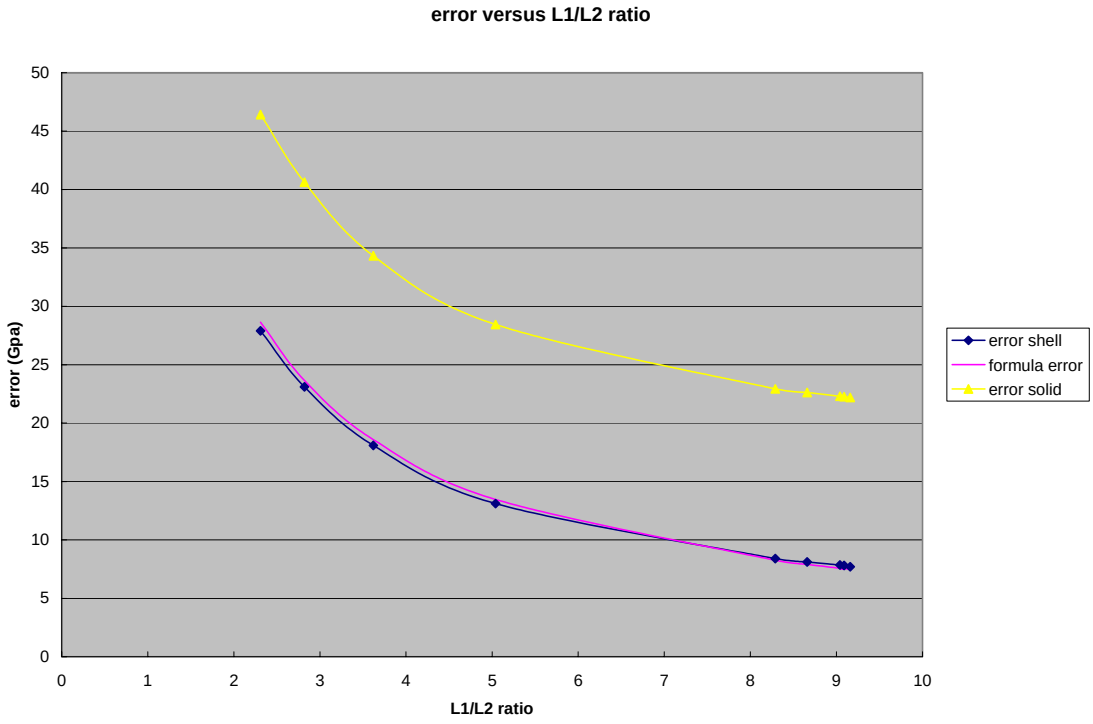

Figure 3.13 The dependence of errors on the length ratio L_1: L_2

Table 3.1 Geometrical parameters of 9 different membranes

	R	S	W_1	W_2	L	L'	L_1	L_2	M/2
	nm	nm	nm	nm	nm	nm	nm	nm	nm
1175A-2I-1	30000	25981	7500	67500	226000	285035	256981	28054	5000
1175A-2I-2	30000	25981	7500	67500	226000	285415	256981	28434	5000
1175A-2I-3	30000	25981	7500	67500	226000	285235	256981	28254	5000
1175A-2I-4	30000	25981	7500	67500	226000	286647	256981	29666	5000
1175A-2I-5	30000	25981	7500	67500	226000	287969	256981	30988	5000
1175A-2I-6	30000	25981	7500	67500	226000	307969	256981	50988	5000
1175A-2I-7	30000	25981	7500	67500	226000	327969	256981	70988	5000
1175A-2I-8	30000	25981	7500	67500	226000	347969	256981	90988	5000
1175A-2I-9	30000	25981	7500	67500	226000	367969	256981	110988	5000

Table 3.2 The elastic modulus and the errors calculated by the simulation results and equation 3.18

	L_1/L_2	E GPa (shell 63)	E GPa (solid 45)	E GPa (formula estimation)	error (shell model)	error (solid model)	error(for mula)
1175A_2I_1	9.16	85.7	100.19	85.47842761	7.7	22.19	7.478427613
1175A_2I_2	9.04	85.85	100.3	85.57649344	7.85	22.3	7.576493443
1175A_2I_3	9.09	85.81	100.26	85.53532182	7.81	22.26	7.535321821
1175A_2I_4	8.66	86.11	100.62	85.90473778	8.11	22.62	7.904737776
1175A_2I_5	8.29	86.4	100.93	86.2528766	8.4	22.93	8.252876604
1175A_2I_6	5.04	91.11	106.44	91.45987921	13.11	28.44	13.45987921
1175A_2I_7	3.62	96.09	112.32	96.58248958	18.09	34.32	18.58248958
1175A_2I_8	2.82	101.1	118.62	101.6542835	23.1	40.62	23.65428355
1175A_2I_9	2.31	105.9	124.41	106.6369894	27.9	46.41	28.63698944

CHAPTER 4
EXPERIMENTAL PROCEDURES

4.1 Sample Preparation

The geometry of specimen is as described in Chapter 3. Specimens with membranes at different types and sizes are designed on a single wafer. Figure 4.1 is a schematic drawing showing the pattern for a 4-inch wafer, consisting of 28 dies in total with different membrane dimensions. In each of the dies, 13 groups of membranes with different dimensions are represented in individual windows named from Group a to Group m, where 5 identical membranes are placed for each group. Actual values for each group are listed in Table 4.1.

4.2 Microfabrication Procedures

The specimens were fabricated on double side polished (100) Si wafers. The suspended membranes were fabricated by a series of microfabrication steps. Figure 4.2 shows the main processes schematically.

To act as etch stops during wet etching and aid in defining the bottom view windows, a layer of 300 nm thick, low-stress silicon nitride was deposited on both sides of the wafer by LPCVD. Low-stress silicon nitride typically has a tensile residual stress below 50 MPa, allowing its application in micromaching as a freestanding film.

After patterning on the bottom side of the wafer using lithography techniques, the bottom windows were then opened by the reactive ion etching using surface technology system advanced oxide etcher. Surface Technology Systems 320 parallel RIE tool uses fluorine chemistry and a high density inductively coupled plasma to etch silicon nitride at a rate up to 0.2 microns per minute. 3000A of Si_3N_4 can be etched with etching rate of 120nm/min using the recipe that CF_4 = 25sccm, O_2 = 5sccm, P = 100W at 13.56 MHz, p = 60mTorr. The driven electrode area is about 900 cm^2. CF_4-based etches typically target silicon dioxide, but this etch was found to etch silicon nitride and silicon even faster than oxide. The addition of oxygen in this recipe increases the oxide etch rate but also increases the photoresist etch rate, significantly reducing the selectivity. The oxygen also reduces fluorocarbon polymer buildup on the chamber walls, yielding a more stable etch rate over time.

Double side alignment is necessary for patterning the topside (the membrane side) of the wafer to align them perfectly with the opening window on the back side of the wafer. About 1 μm thick of positive photoresist AZ5214 was spin coated onto the wafer and patterned using standard lithography techniques before any metal film deposition. E-beam evaporation or sputtering deposition is employed to deposit films. A layer of 20nm of Ti or Cr should be deposited prior to the metal film as an adhesion layer between film and the substrate.

The final pattern of the membranes is obtained by the lift off process, which usually requires soaking the wafers in acetone for 5 minutes of ultrasonic with mild agitation. After the 5 minutes some mechanical assistance with a clean room swab may be necessary. This is to ensure that the silver in the acetone did not redeposit onto the wafers.

Bottom view windows are opened by wet etching of Si. A Teflon wafer holder made by AMMT was used to protect the top surface of the wafer during wet etching of Si. Anisotropic silicon etching is performed in 30wt% KOH etchant at a temperature of 80^{o}C. KOH etches silicon depending on the concentration of the KOH solution and temperature. Figure 4.3 is provided for the etch rates depending on temperature (in degrees Celsius) for various solution concentrations [40]. Experimentes have shown that solutions less than 30% KOH yield rough etching as in Figure 4.4 [41]. Addition of isopropyl alcohol has been found to decrease the etch rate by approximately 20%. Data of etch rates at different KOH concentration and temperatures and different silicon doping levels, as well as etch-stop mechanisms, have been documented by Seidel et al [42]. The anisotropic etch geometry (side view) is shown in Figure 4.5.

The membranes are released by etching the silicon nitride underneath using hot phosphoric acid etching. Phosphoric acid (85% by weight) at 160 ^{o}C is one of the few wet etches for silicon nitride. It also can be released by reaction ion etching in the STS system. The detail fabrication issues are discussed in the next chapter.

4.3 Experimental Setup and Test Methodology

The nanoindenter in the membrane deflection experiment set-up is used to apply a line load to the center of the specimen from the top, and in order for that, a test flow has to be designed and programmed to control the nanoindenter to perform in such a desired way. Another part of the experiment setup is a Mirau microscope interferometer which should be positioned directly below the specimen to independently measure deflection of the membranes through the microfabricated die window. Figure 4.6 shows the

microscope interferometer incorporated with a five axis manipulation component and a CCD camera onto the customized working stage. This component will finally integrate with the nanoindenter unit to realize the microscale mechanical plasticity testing.

The typical experimental procedure can be described in three steps: The first step is to locate and characterize the membrane geometry by means of the optical microscopy and interferometry. Once the dimensions and surface profile are stored, the sample die is moved to the nanoindenter to begin the second step by means of an x-y translation stage with a positioning accuracy of less than 1μm. The second step is the membrane deflection experiment involving deflection of the membrane by the nanoindenter. Parameters are set and the instrument performs a drift test. Once the test criterion is reached, the membrane is loaded. Simultaneously, the aligned interferometric station is focused on the back surface of the film. The camera is then set to obtain digital images within a desired period of time. Force and displacement data are stored in the nanoindenter controller PC, and full field displacements are stored by acquiring monochromatic images. Prior to acquiring each set of images, the focus on the surface is updated to correct for the out-of-plane motion resulting from the downward displacement of the membrane. The third step of the experiment is data reduction. The data directly obtained from the MDE test must then be reduced to get the stress-strain curves for the membrane. The load in the plane of the membrane is found to be a component of the vertical nanoindenter load. Therefore, using the measured distance between fringes, obtained from the interferometer, and load, Cauchy stress and strain are independently computed [15, 36].

4.3.1 Alignment

It is crucial that the membrane is loaded in a uniform manner to avoid spurious effects resulting from torsional forces and errors in true deflection. It is important that the nanoindenter line-load tip, membrane, and interferometer are all in alignment. To align the membrane with the interferometer is the first step. Adjust the x- and y-axis rotation until all the fringes disappear. Second step in alignment is to align the membrane with the nanoindenter line-load tip. The stage may need to be adjusted to achieve the alignment. Membrane is deflected by a modest amount to develop a few fringes to check alignment. The appropriate direction in which the stage should be rotated around the x-axis is determined by observing the fringes on the contact area of the membrane. The interferometer is realigned with the membrane until all fringes are developed uniformly.

4.3.2 Fringe Development and Measurement

The principle of fringe development has been discussed in chapter 3. By acquiring images at periodic intervals, the deflection and strain can be mapped as a function of time. Another method for strain measurement is to use nanoindenter to record the displacement history of the indenter tip. Much like the interferometer, this data also provides an overall strain for the specimen. However the nanoindenter method lacks some key aspects provided by the interferometer data.

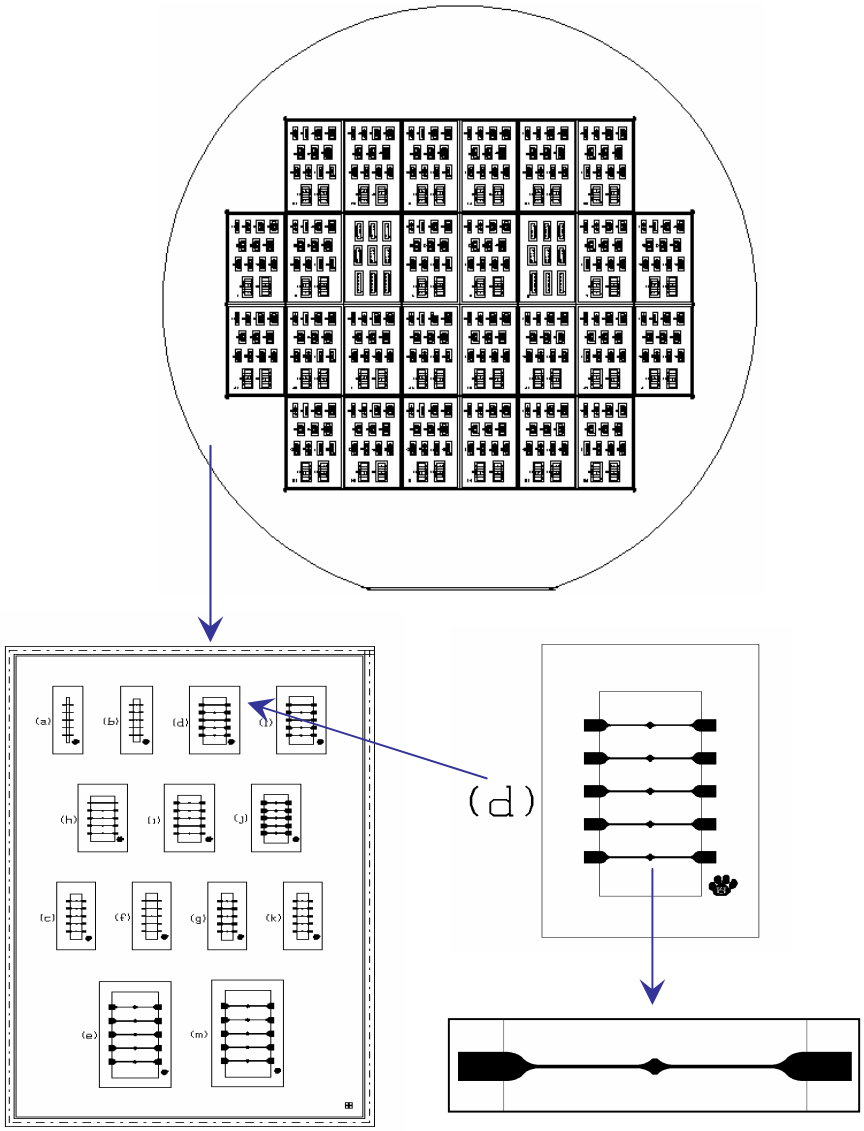

Figure 4.1 Schematic representations of the wafer and the die layout of differently shaped group of membranes.

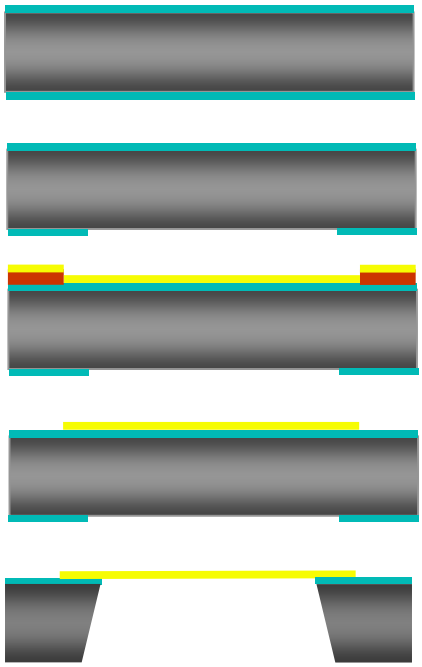

Figure 4.2 Schematic of microfabrication processes.

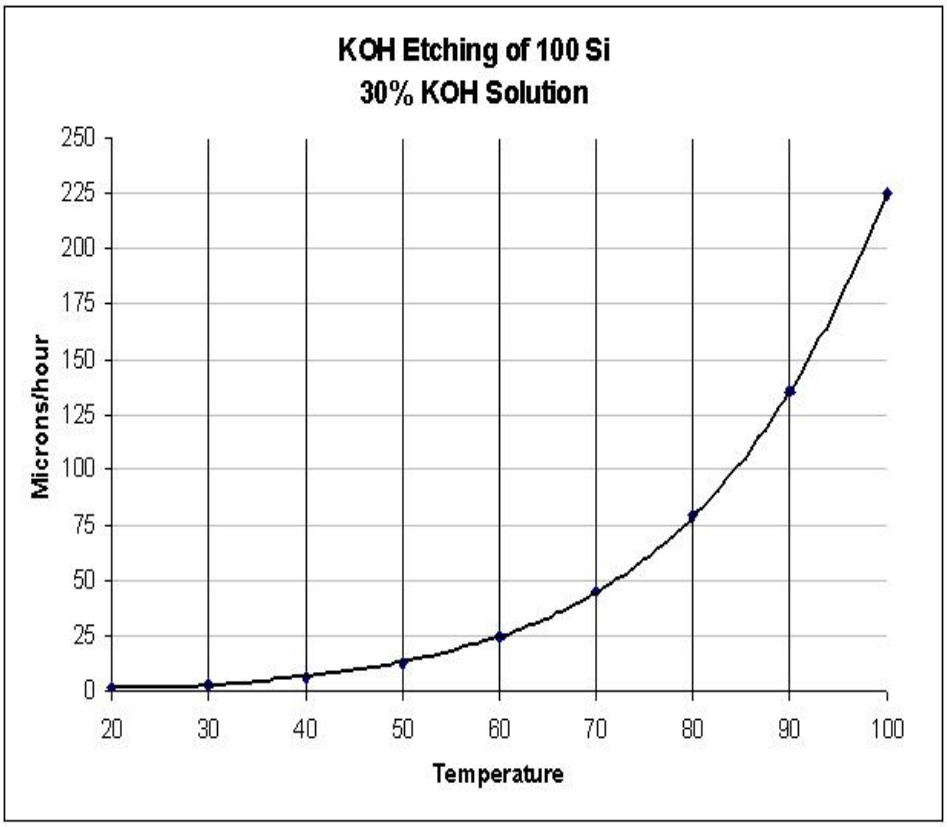

Figure 4.3 Etch rates versus temperature for 30% KOH solution [43]

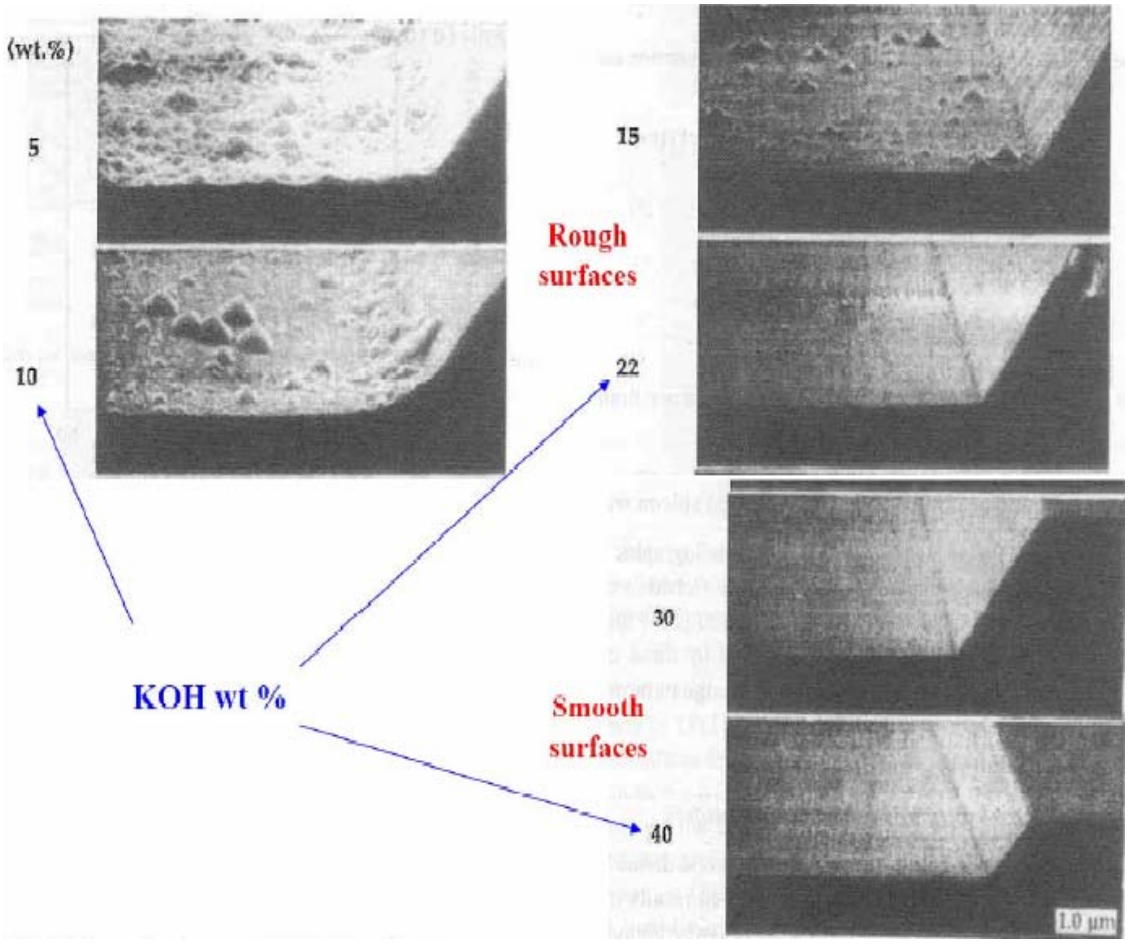

Figure 4.4 Surface roughness for different KOH concentrations [41].

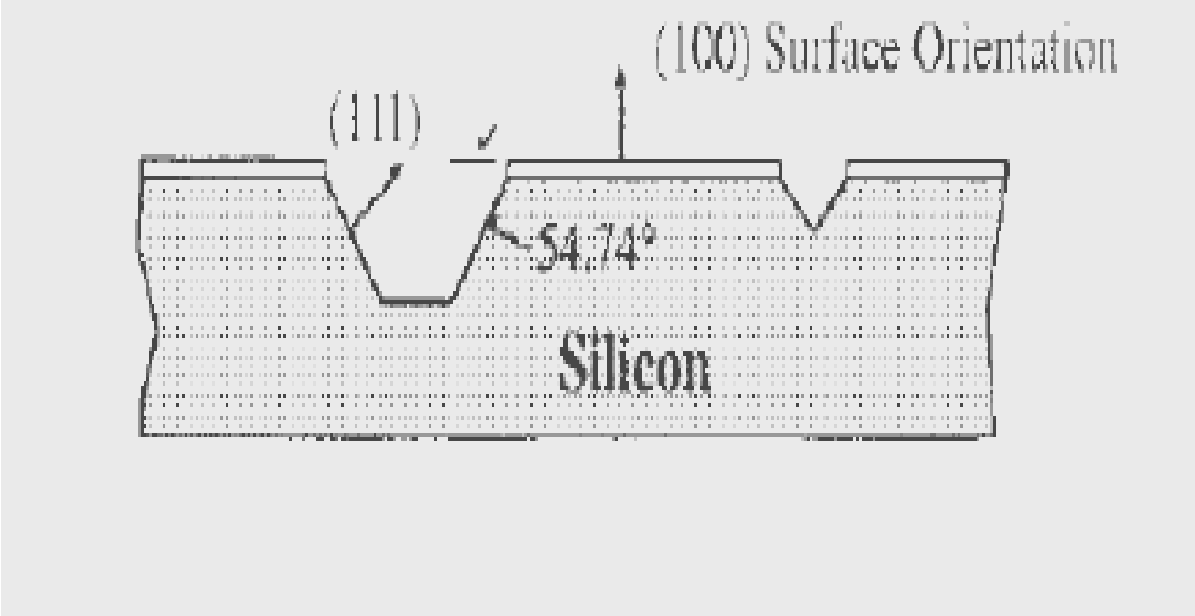

Figure 4.5 The anisotropic etch geometry (side view) of silicon [41].

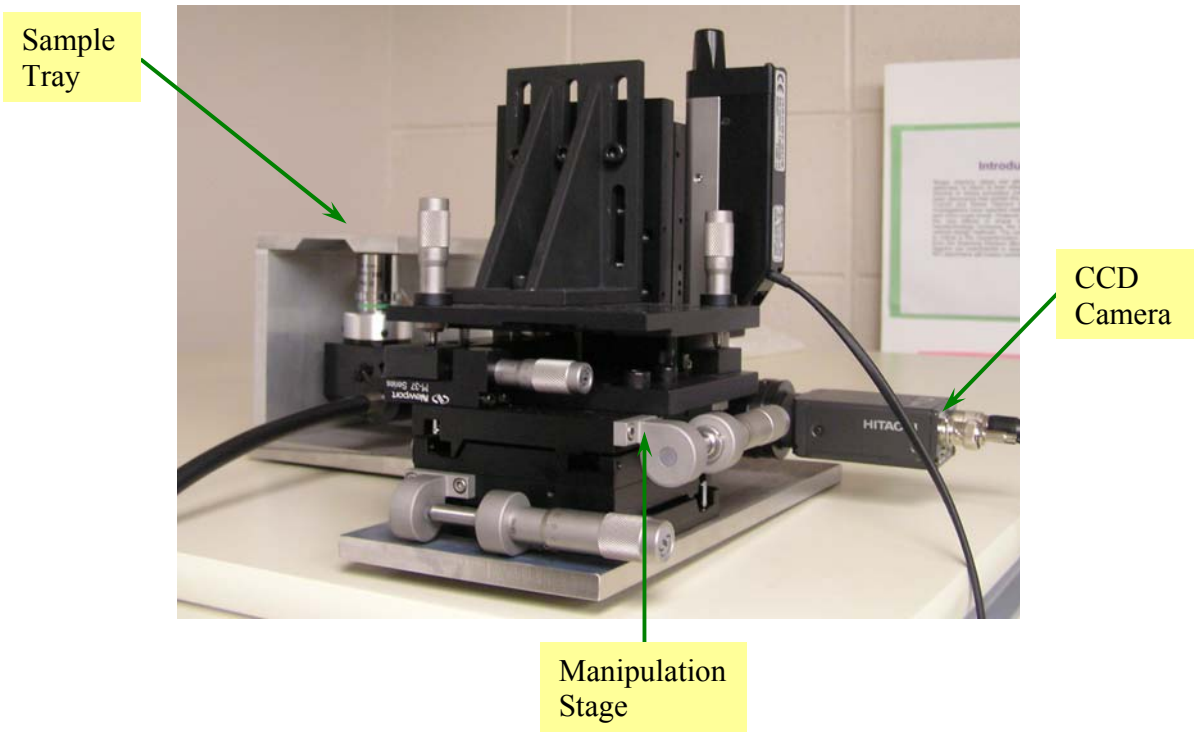

Figure 4.6 The interferometer set up.

Table 4.1 Membrane dimensions for different sized specimens in each die.

Sample	Dimensions (μm)						
	W	L	L/W	D	E	R	N
Group a	1.25	25	20	286.7	11.25	5	100
Group b	2.5	50	20	361.9	22.5	10	100
Group c	5	100	20	513.8	45	20	100
Group d	10	200	20	817.9	90	40	100
Group e	20	400	20	1424	180	80	100
Group f	2.5	126	50	513.9	22.5	10	100
Group g	7.5	74	10	514	67.5	30	100
Group h	5	252	50	817.8	45	20	100
Group I	7.5	226	30	818	67.5	30	100
Group j	15	148	10	818	135	60	100
Group k	5	100	20	513.8	45	20	100
Group l	10	200	20	817.9	90	40	100
Group m	20	400	20	1424	180	80	100

CHAPTER 5

RESULTS AND DISCUSIIONS

5.1 Microfabrication Issues of Free Standing Thin Films

As stated in Section 4.2, the membranes were released by etching the silicon nitride underneath using hot phosphoric acid. Phosphoric acid (85% by weight) at 160 ^{o}C is one of the few wet etches for silicon nitride. The etching was performed by putting the dies in the beaker with hot phosphoric acid. The lid on top of the beaker is used to maintain the etching temperature. The etch rate, which is very sensitive to temperature, was about 4.5nm/min for silicon-rich, low-stress silicon nitride at 160 ^{o}C.

Another method to etch silicon nitride was also performed by using inductively coupled plasma (ICP) etcher STS AOE (Advance oxide etcher). It is a method of material removal with high aspect ratio by plasma etching using an inductively coupled RF source. The substrate is RF-biased independent of the inductively coupled RF plasma, which results in low ion energies and thus low ion bombardment. Consequently, an ICP system will provide high chemical etch selectivity with high etch rates. The 13.56 MHz RF system produces a high-density, low- pressure, low-energy inductively coupled plasma. This type of plasma allows high selectivity and aspect ratio etching for depths greater than 250 microns. The system control is via a standard PC, which automatically loads a

wafer into the process chamber. Once in the chamber, the wafer is placed onto a helium-cooled chuck during the process.

Using the recipe of CF_4 (25sccm) and O_2 (2sccm) to etch the silicon nitride, the oxygen flow can cause metallic silver change to silver oxide. It has been studied that the oxygen flow rate played an important role in the formation of silver oxide thin films. Silver oxide thin films form with oxygen flow rates varied in the range 0.00-2.01 sccm by DC magnetron sputtering of silver thin films [44]. With the presence of oxygen and the similar operating principle in the reactive ion etching, silver has been changed to silver oxides during the etching of silicon nitride. With the recipe of pure CF_4 to etch the silicon nitride, a polymer layer is formed on the membrane as a result of the flux of polymer precursors, atomic fluorine, and energetic particles to the etched surface.

Another problem occurred for the 4 inch wafer to fit in the STS AOE etcher. The system is designed to etch a 125 mm (5 in.) wafer. Four inch wafer used in this experiment is taped on the five inch wafer by using Kapton tape which can withstand temperature up to 500°F. The five inch wafer is spin coated with AZ5214 photo-resist at 1000 rpm for 10 seconds. The thin layer of photo-resist can protect the five inch wafer being etched thus make it reusable. It is found that the yield of the silver free-standing membranes was relatively low because the silver membranes are in direct contact with the five inch wafer surface. After removing the tape on the four inch wafer, the membranes are inclined to stick on the five inch wafer surface thus are easy to break. In order to avoid the direct contact of membranes with five inch wafer, a specific die holder was designed to hold the dies of the four inch wafer in the STS AOE etcher. As the top view shown in Figure 5.1, five holes of identical sizes were etched 150 um deep from the

silicon surface using STS ASE (Advanced Silcion Etcher) on a four inch wafer as die holders. The geometry of the holes was designed slightly in a smaller size to make sure the membranes not in contact with any surface. The dies were taped to the holder with the membranes facing to the holes. A side view of the die holder and the position of the dies are shown in Figure 5.2.

Concerning the issue that silver thin films can be easily oxidized in the surface technology system; dies were painted with thin layer AZ5214 photo-resist to protect the membranes being oxidized. As photo-resist is hardly attacked by plasma in the STS AOE system, membranes are well protected with photo-resist. After the nitride etching, photo-resist was removed with acetone to release the free-standing thin films.

5.2 Characterization of Silver Thin Films

Many techniques can be used to characterize thin films. Scanning Electron Microscopy (SEM) uses a focused electron beam to scan small areas of solid samples. Secondary electrons are emitted from the sample and are collected to create an area map of the secondary emissions. Since the intensity of secondary electron emission is very dependent on local morphology, the area map is a magnified image of the sample surface. Spatial resolution is as high as 1 nanometer for some instruments, but 4 nm is typical for most. Magnification factors can exceed 500,000. Backscattered electrons (BE) and characteristic X-rays are also generated by the scanning beam and many instruments can utilize these signals for compositional analysis of microscopically small portions of the sample. Scanning electron microscopy (SEM) is employed to characterize grain size and

morphology of the membranes before testing, both across the width of the gauged region as well as through the thickness.

Since silver thin films are obviously conductive, we used 20 kV as the gun voltage. Figure 5.3 (a) and (b) show the typical SEM images of 1um silver thin film surface without and with hot phosphoric acid etching, respectively. Before the etching, the average grain size was about 150 nm. After the hot etching at 160 ^{o}C, the grain size increased obviously and it became one or several microns.

It is known that heating may promote grain growth. Because of the high temperature, a few grains that first lose or overcome the restraints grow rapidly and consume other neighbors to minimize the interface energy, surface energy or strain energy. Therefore it proceeds by the gradual elimination of small grains with unfavorable shapes or orientations relative to their neighbors. For alloys, such grain growth is greatly restricted by finely divided impurity phases and by intermetallic compounds of elements, such as manganese and chromium that slows down the process by pinning the grain boundaries, and preventing their further movement. Generally, these grains grow only at very high temperatures and may attain diameters of several inches. However, in this study, high-purity silver thin films are characterized. The restraints due to the impurity are greatly reduced. It is being reported after annealing at 81 ^{0}C the grain size of silver thin films have greatly increased [45].Therefore, at temperature of 160 ^{0}C, relatively large grain growth is observed, as shown in Figure 5.3 (b).

5.3 Experimental Data

5.3.1 Data Reduction

In the membrane deflection test, the data recorded is in raw form and must be processed to obtain the load and stress. The data obtained for a test typically are composed of the nanoindenter displacement, load and time as well as video file of the fringe development.

Two main steps are required for reduction of the data. Correction of the raw load obtained from the nanoindenter is the first step. It is followed by the calculation of the membrane in-plane load as a second step. The raw load signature also includes other factors such as stiffness of the gantry, stiffness of the support springs, and variability in the resistivity of the load coil, and the thermal drift of the column. Among those factors, the influence of gantry stiffness and load coil resistance change are normally considered to be negligible. The combined effect of the support spring stiffness and thermal drift results in a load response significantly larger than that of the typical membrane. The stiffness of the support springs is the largest contribution to this problem and it must be measured before the tip is in contact with the membrane. The test is performed in the air prior to deflecting the membrane.

Actual membrane deflection was immediately performed after the air tests. The actual load response of the membrane is determined by comparing load-deflection signatures with final air test. A polynomial representation of the load-displacement signature of the air test is made at the initial step. The polynomial is then subtracted from the membrane's vertical load-displacement signature to eliminate thermal drift and spring

stiffness effects. Vertical-load-displacement signatures of raw data of 0.5um silver membranes are shown in Figure 5.4.

5.3.2 Stress-strain Curves

Stress-strain curves for the 0.5μm thick membrane (Group M) releasing by AOE etching of silicon nitride are shown in Figure 5.5. The elastic behavior of membranes in the same group have represented measured young's modulus in a range of 106-110 GPa.The measured elastic modulus is higher than the value of 83 GPa for bulk silver. The reported elastic modulus for silver thin films varied from 63-78GPa [46, 47, 48].

The elastic behavior of the 0.5 μm thick membrane released by hot phosphoric acid etching of silicon nitride shows a measured young's modulus of 54-58GPa. The stress-strain curves of membranes (Group M) are shown in Figure 5.6. The significant change of stress on membranes with increasing strain occurs as the membranes begin to deform plastically. The failure of the membranes is not a sharp loss on membrane load; however it showed a gradual decrease in stress with the increase in strain. Jogs seen in the stress-strain curves indicated the effect of shear localization. In general, the shear localization process involves initiation and growth where initiations are expected to be a stochastic process in material space where anisotropy in the elastic-plastic behavior of single crystals and intercrystalline interactions serve to form natural perturbations to the material's local stability. Proposed mechanism for shear localization may results from the greater grain size after the hot phosphoric acid etching at 160^{o}C. The stress-strain curves of membrane of different half length (Group I) are also shown in Figure 5.7. They have shown the mechanical behavior of elastic modulus of 40-45GPa.

Mechanical behaviors for the 1μm thick membrane (Group M) released by AOE etching of silicon nitride are shown in the stress-strain curves in Figure 5.8. The measured young's modulus is in a range of 106-130GPa.

The stress-strain curves in Figure 5.9 for 1μm thick membrane (Group M) released by hot phosphoric acid etching of silicon nitride have shown the elastic modulus in the range of 49-60GPa.

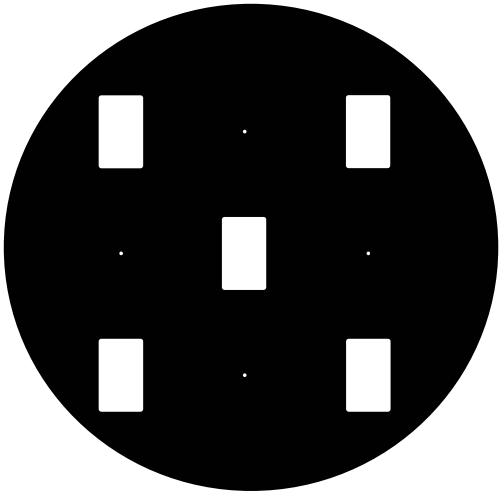

Figure 5.1 Top view of the die holder with five identically sized holes

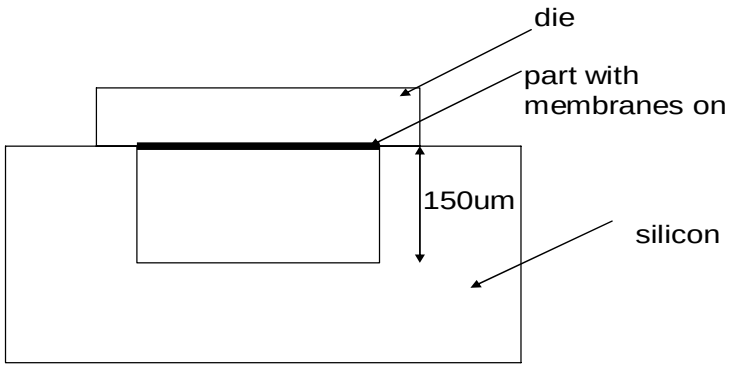

Figure 5.2 Side view of the die holder

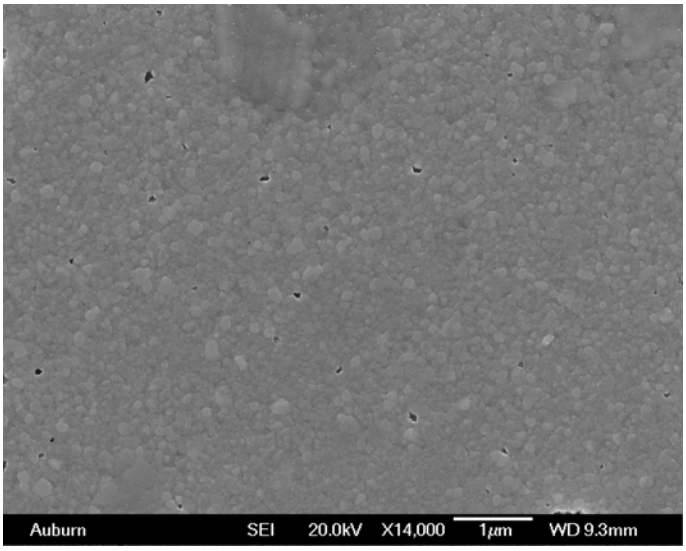

(a)

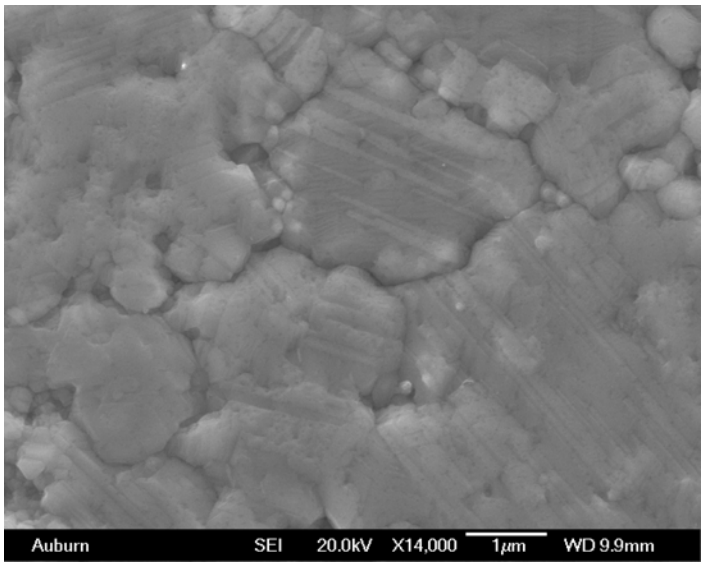

(b)

Figure 5.3 SEM image of 1um silver thin film surface without nitride etching (a) SEM image of 1um silver thin film surface after hot phosphoric acid etching of silicon nitride (b)

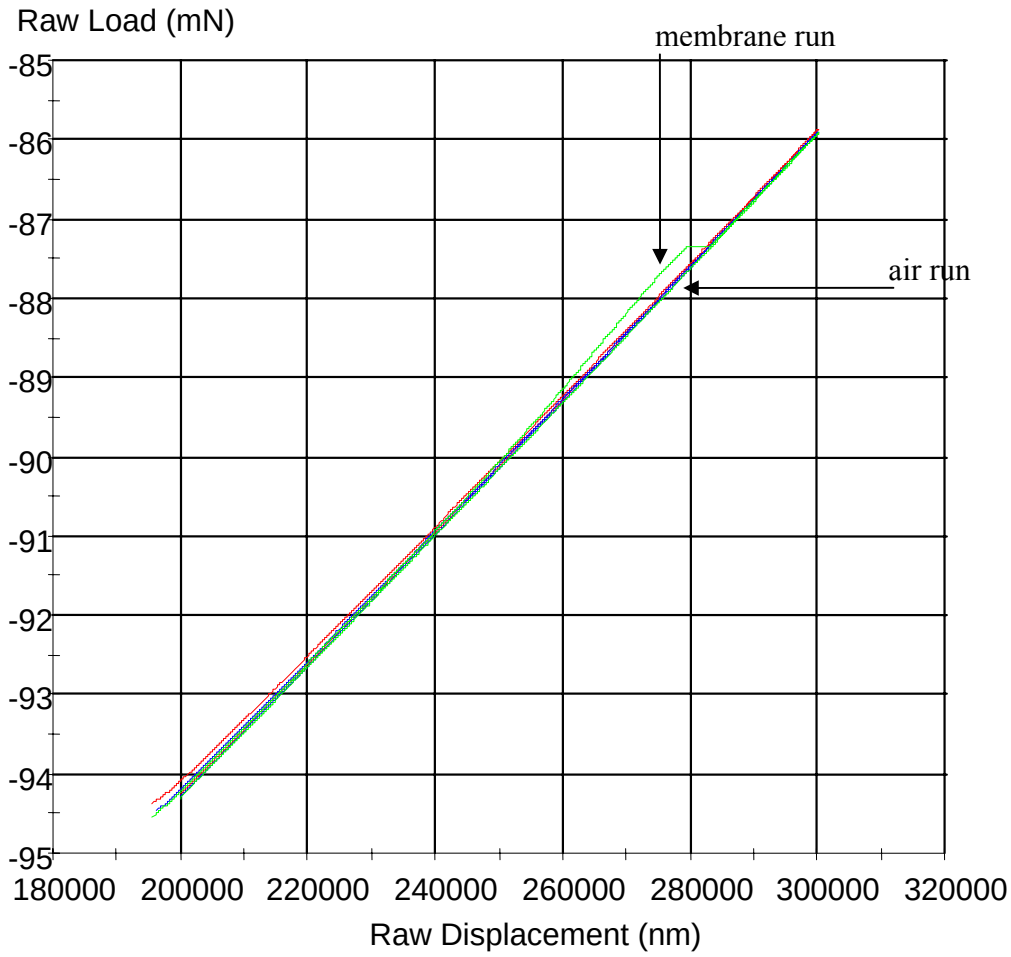

Figure 5.4 Plot of raw load vs. displacement for air runs and membrane run for 1um silver thin film using AOE etching of silicon nitride.

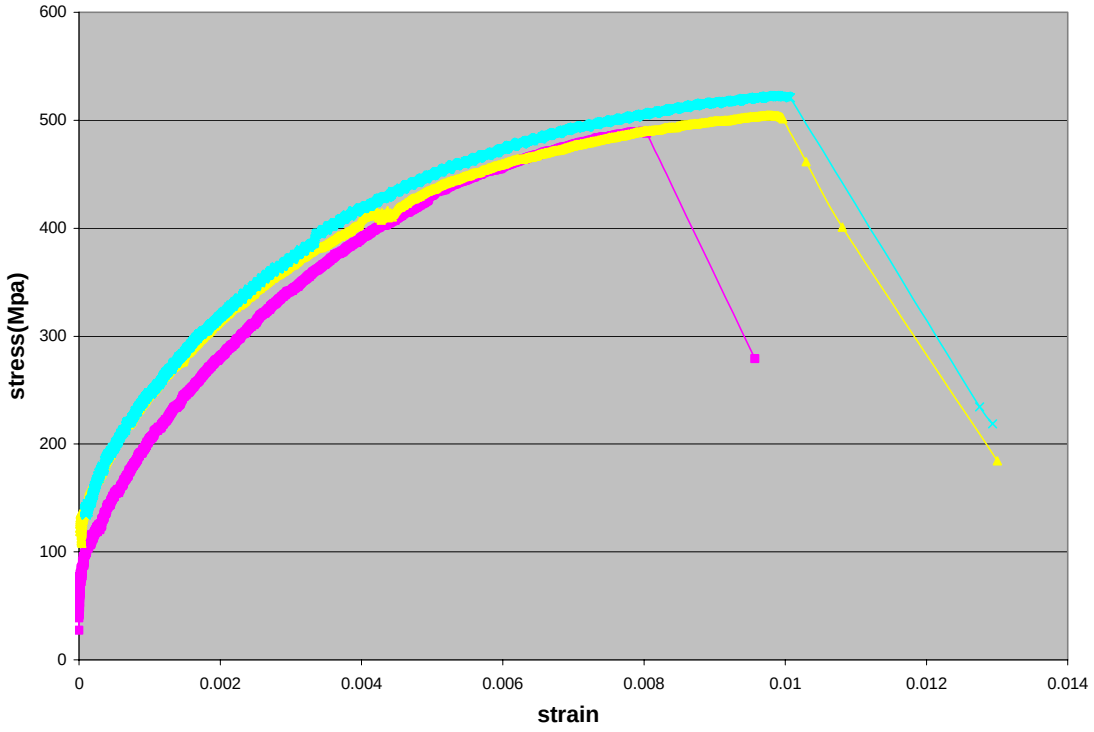

Figure 5.5 Stress-strain curves of silver membranes (group M) with film thickness of 0.5 μm using AOE etching of silicon nitride.

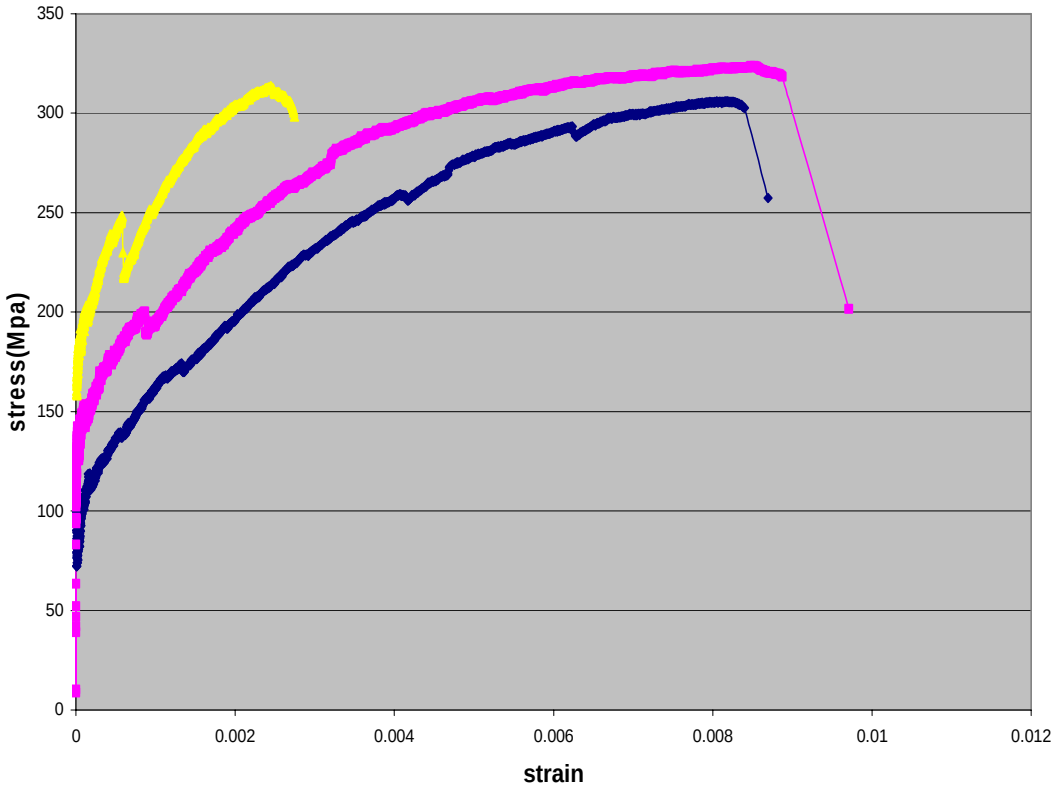

Figure 5.6 Stress-strain curves of silver membranes (group M) with film thickness of 0.5 μm using hot phosphoric acid etching of silicon nitride.

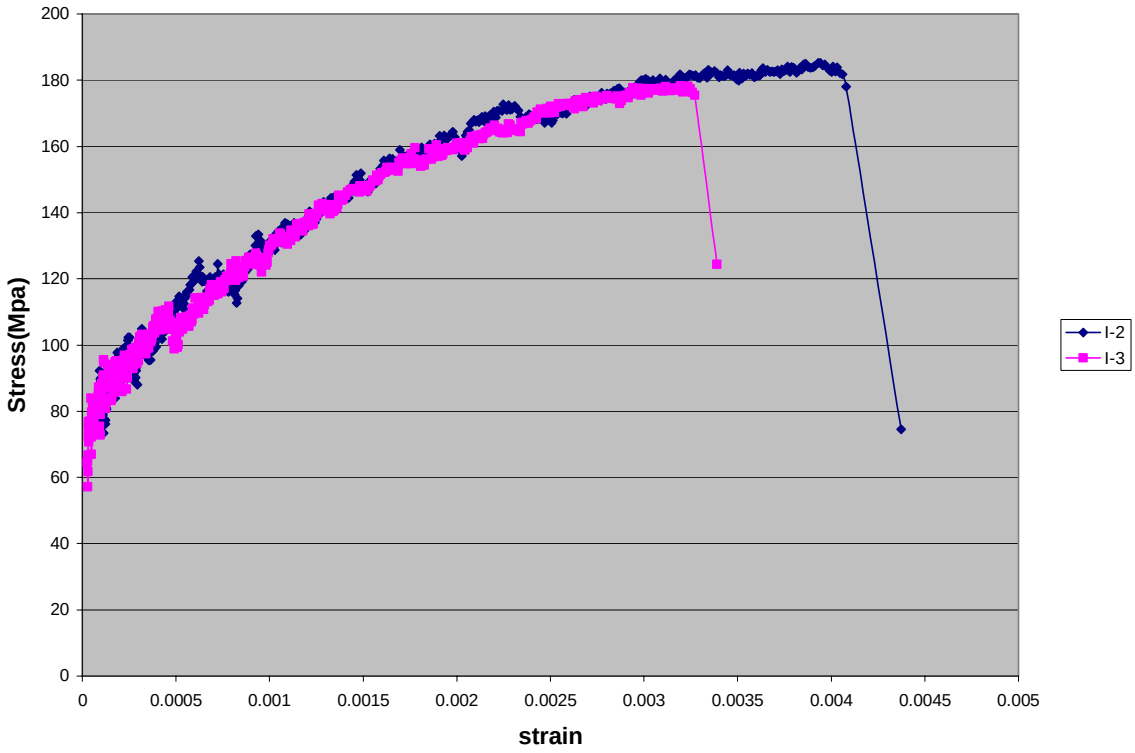

Figure 5.7 Stress-strain curves of silver membranes (group M) with film thickness of 0.5 μm using hot phosphoric acid etching of silicon nitride.

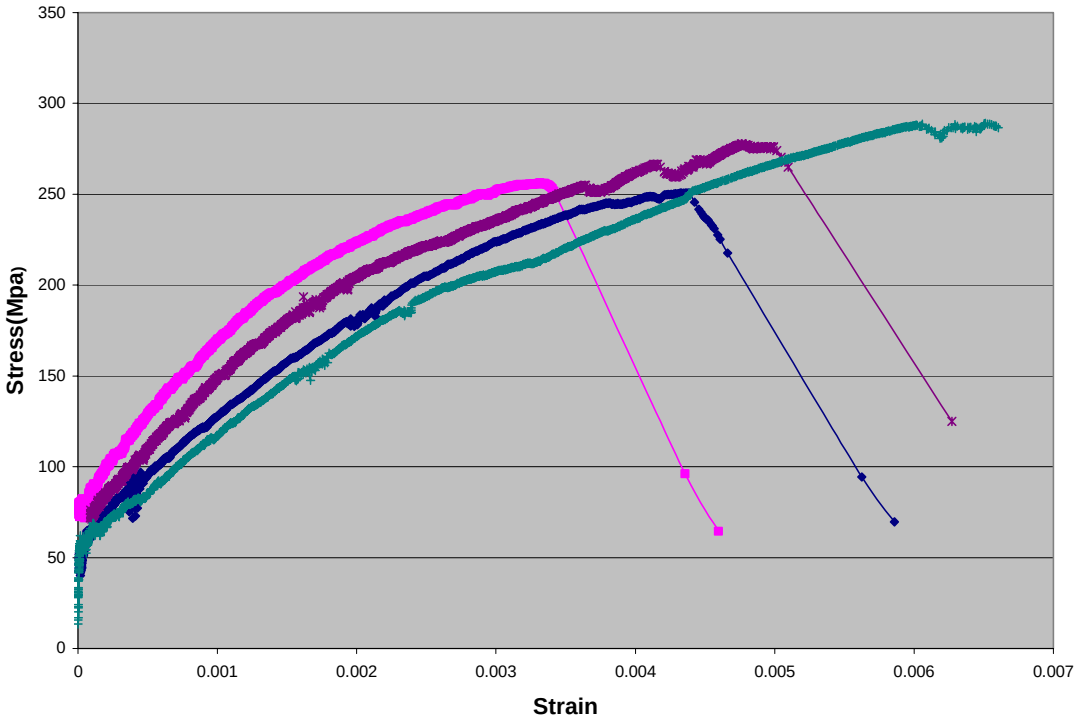

Figure 5.8 Stress-strain curves of silver membranes (group M) with film thickness of 1 μm using AOE etching of silicon nitride.

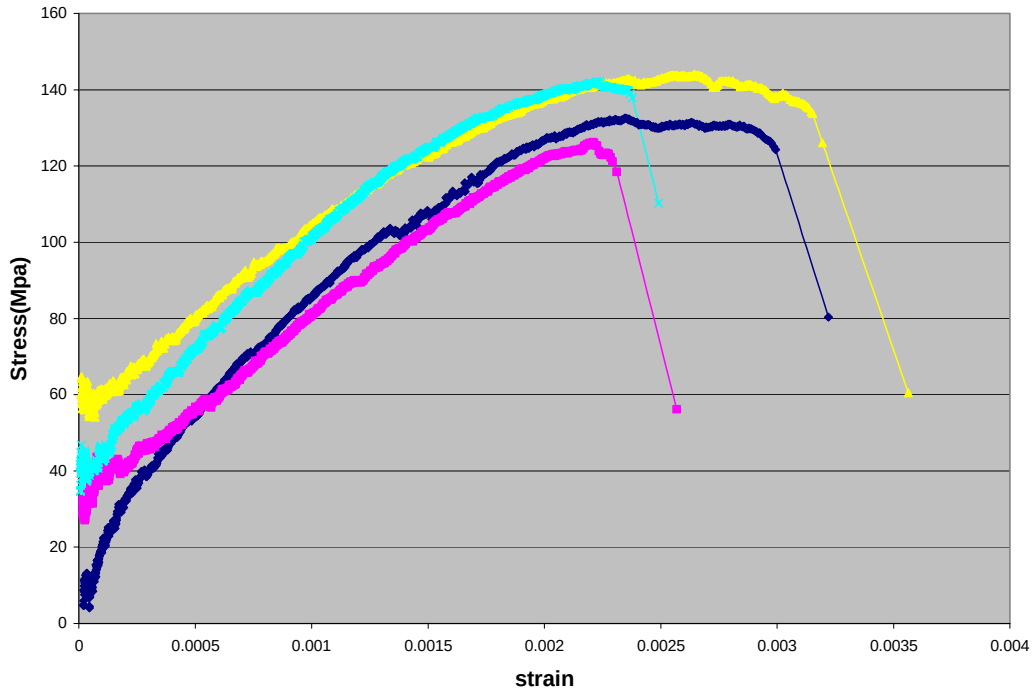

Figure 5.9 Stress-strain curves of silver membranes (group M) with film thickness of 1 μm using hot phosphoric acid etching of silicon nitride.

CHAPTER 6

CONCLUSIONS AND FUTURE WORKS

The preceding chapters have reviewed different testing methods for mechanical properties of thin films as microtensile test and MEMS based test. Membrane deflection test is well studied to investigate the mechanical properties for polycrystalline metal thin films. Numerical simulationS by ANSYS software of membranes with different bottom window sizes show the overestimation of elastic modulus while using the gauge width to calculate the elastic modulus. The numerical simulation results agree with the simply analytical solution.

The experimental parts include the fabrication and membrane deflection test of 0.5 μm and 1μm silver free standing thin films. The fabrication issues involved the release of silver membranes by etching the silicon nitride underneath the membranes. Two methods to etch silicon nitride are performed by using inductively coupled plasma (ICP) etcher STS AOE (Advance oxide etcher) and by hot phosphoric acid etching. The SEM images have shown the grain growth during the hot phosphoric acid etching. A specific die holder is design and fabricated to protect the membranes in order to improve the yield. Photoresist has been painted on each dies to prevent silver thin film from being oxidized due to the oxygen flow in the AOE etcher. 0.5 μm and 1μm silver free standing thin films have been successfully fabricated. The mechanical behavior of silver free-standing thin films released by AOE and hot acid etching show a discrepancy. It may be

contributed to the texture change due to heat treatment of silver thin film during hot phosphoric acid etching. Also shear localization is observed in the deformation process of silver thin film with hot phosphoric acid etching.

In the future, high-resolution electron backscattered diffraction (EBSD) in a field-emission SEM will be used to obtain the information about film texture and grain orientation, which will provide an insight of how the varying microstructures of the limited number of grains in a given volume affect the mechanical deformation behavior. This may give us new insight to the texture for the silver thin films and how it is related to the mechanical behaviors. Also annealing of silver thin films is designed at 160^{o}C for 75 minutes to mimic the heat treatment of hot phosphoric acid etching. EBSD is also used to investigate the possible texture change of the films.

Fracture observation of silver thin films is also of great interest to investigate the fracture mechanism. SEM and TEM images can be used to show the deformation bands and proposed mechanism for shear localization

BIBLIOGRAPHY

1. Fleck, N.A. and J.W. Hutchinson, *Strain gradient plasticity*, in *Advances in Applied Mechanics, Vol 33*. 1997. p. 295-361.
2. Stolken, J.S. and A.G. Evans, *A microbend test method for measuring the plasticity length scale.* Acta Materialia, 1998. **46**(14): p. 5109-5115.
3. Poole, W.J., M.F. Ashby, and N.A. Fleck, *Micro-hardness of annealed and work-hardened copper polycrystals.* Scripta Materialia, 1996. **34**(4): p. 559-564.
4. Pharr, G.M., *Instrumented Indentation Testing*, in *ASM Handbook*. 2000. p. 232-243.
5. C. B. Ponton, R.D.R., *Study of the Effect of the Indentation Time and Load on Fracture Toughness and Crack Morphologies in WC-17Co Thermally Sprayed HVOF Coating.* Mater. Sci. Technol., 1989. **5**: p. 865.
6. Y.Y. Lim, M.M.C., Y. Enomoto, *Accurate determination of the mechanical properties of thin aluminum films deposited on sapphire flats using nanoindentations.* Journal of Materials Research, 1999. **14**: p. 2314.
7. T.Y. Tsui, G.M.P., *Substrate effects on nanoindentation mechanical property measurement of soft films on hard substrates.* Journal of Materials Research, 1999. **14**: p. 292.
8. Saha, R. and W.D. Nix, *Effects of the substrate on the determination of thin film mechanical properties by nanoindentation.* Acta Materialia, 2002. **50**(1): p. 23-38.
9. Beams, J.W., *Structure and properties of thin films*. 1959: Wiley.
10. Brotzen, F.R., *Mechanical Testing of Thin-Films.* International Materials Reviews, 1994. **39**(1): p. 24-45.
11. Kraft, O. and C.A. Volkert, *Mechanical testing of thin films and small structures.* Advanced Engineering Materials, 2001. **3**(3): p. 99-110.
12. Tsuchiya, T., et al., *Specimen size effect of tensile strength of surface-micromachined polycrystalline silicon thin films.* Journal of Microelectromechanical Systems, 1998. **7**(1): p. 106-113.
13. Ruud, J.A., et al., *A New Method for Tensile Testing of Thin-Films.* Journal of Materials Research, 1993. **8**(1): p. 112-117.
14. Greek, S., et al., *In situ tensile strength measurement and Weibull analysis of thick film and thin film micromachined polysilicon structures.* Thin Solid Films, 1997. **292**(1-2): p. 247-254.
15. Espinosa, H.D. and B.C. Prorok. *Size effects of the mechanical behavior of this gold films*. in *Proceedings of the Symposium on Mechanical Properties of MEMS Structures, International Mechanical Engineering Congress*. 2001. New York, New York.

16. Espinosa, H.D., B.C. Prorok, and M. Fischer, *A methodology for determining mechanical properties of freestanding thin films and MEMS materials.* Journal of the Mechanics and Physics of Solids, 2003. **51**(1): p. 47-67.
17. Espinosa, H.D., B.C. Prorok, and B. Peng, *Size effects in submicron gold films subjected to uniaxial tension.* submitted, Journal of the Mechanics and Physics of Solids, 2003.
18. Haque, M.A. and M.T.A. Saif, *A review of MEMS-based microscale and nanoscale tensile and bending testing.* Experimental Mechanics, 2003. **43**(3): p. 248-255.
19. Sharpe, W.N., et al., *Effect of specimen size on Young's modulus and fracture strength of polysilicon.* Journal of Microelectromechanical Systems, 2001. **10**(3): p. 317-326.
20. Fleck, N.A., et al., *Strain Gradient Plasticity - Theory and Experiment.* Acta Metallurgica Et Materialia, 1994. **42**(2): p. 475-487.
21. Ma, Q. and D.R. Clarke, *Size-Dependent Hardness of Silver Single-Crystals.* Journal of Materials Research, 1995. **10**(4): p. 853-863.
22. McElhaney, K.W., J.J. Vlassak, and W.D. Nix, *Determination of indenter tip geometry and indentation contact area for depth-sensing indentation experiments.* Journal of Materials Research, 1998. **13**(5): p. 1300-1306.
23. Huber, N., W.D. Nix, and H. Gao, *Identification of elastic-plastic material parameters from pyramidal indentation of thin films.* Proceedings of the Royal Society of London Series a- Mathematical Physical and Engineering Sciences, 2002. **458**(2023): p. 1593-1620.
24. Stelmashenko, N.A., et al., *Microindentations on W and Mo Oriented Single-Crystals - an Stm Study.* Acta Metallurgica Et Materialia, 1993. **41**(10): p. 2855-2865.
25. De Guzman, M.S., et al. *The Role of Indentation Depth of the Measured Hardness of Materials*. in *Mater. Res. Soc. Symp.* 1993.
26. Busso, E.P., F.T. Meissonnier, and N.P. O'Dowd, *Gradient-dependent deformation of two-phase single crystals.* Journal of the Mechanics and Physics of Solids, 2000. **48**(11): p. 2333-2361.
27. Arsenlis, A. and D.M. Parks, *Crystallographic aspects of geometrically-necessary and statistically-stored dislocation density.* Acta Materialia, 1999. **47**(5): p. 1597-1611.
28. Kroner, E., *Dislocations and continuum mechanics.* Appl. Mech. Rev, 1962. **15**: p. 599–606.
29. Ashby, M.F., *Deformation of Plastically Non-Homogeneous Materials.* Philosophical Magazine, 1970. **21**(170): p. 399-&.
30. Venables, J.A., *Nucleation + Propagation of Deformation Twins.* Journal of Physics and Chemistry of Solids, 1964. **25**(7): p. 693-&.
31. Coutrney, T.H., *Mechanical Behavior of Materials*. 1990, New York: McGraw Hill. 60.

32. Mohamed, S.H., et al., *Effect of annealing and In content on the properties of electron beam evaporated ZnO films.* European Physical Journal-Applied Physics, 2005. **31**(2): p. 95-99.
33. Kim, C., S. Kim, and C. Lee, *Effects of RF power and substrate temperature during RF magnetron sputtering on crystal quality of ZnO thin films.* Japanese Journal of Applied Physics Part 1-Regular Papers Brief Communications & Review Papers, 2005. **44**(12): p. 8501-8503.
34. Thompson, C.V., *The Yield Stress of Polycrystalline Thin-Films.* Journal of Materials Research, 1993. **8**(2): p. 237-238.
35. Espinosa, H.D. and B.C. Prorok. *Size Effects and Passivation Effects on the Plasticity of Freestanding Submicron Gold Films*. in *Proceedings of the SEM Annual Conference on Experimental and Applied Mechanics*. 2002. Milwaukee, Wisconsin.
36. Espinosa, H.D. and B.C. Prorok, *Effects of film thickness on the yielding behavior of polycrystalline gold films.* Materials Research Society Symposium Proceedings, 2001. **688**.
37. Hohenberg, P. and W. Kohn, *Inhomogeneous electron gas.* Phyical Review B, 1964. **136**: p. 864.
38. Messier, R., A.P. Giri, and R.A. Roy, *Revised Structure Zone Model for Thin-Film Physical Structure.* Journal of Vacuum Science & Technology a-Vacuum Surfaces and Films, 1984. **2**(2): p. 500-503.
39. Prorok, B.C., *Micro- and Nanomechanics*. Encyclopedia of Nanoscience and Nanotechnology. Vol. 5. 2004: American Scientific Publishers. 555-600.
40. Seidel, H., et al., *Anisotropic Etching of Crystalline Silicon in Alkaline-Solutions .1. Orientation Dependence and Behavior of Passivation Layers.* Journal of the Electrochemical Society, 1990. **137**(11): p. 3612-3626.
41. Divan, R., N. Moldoven, and H. Camon, *Roughening and smoothing dynamics during KOH silicon etching.* Sensors and Actuators a-Physical, 1999. **74**(1-3): p. 18-23.
42. Seidel, H., et al., *Anisotropic Etching of Crystalline Silicon in Alkaline-Solutions .2. Influence of Dopants.* Journal of the Electrochemical Society, 1990. **137**(11): p. 3626-3632.
43. Seidel, H., et al., *The Effect of Low-Frequency Whole-Body Vibration under Different Visual Conditions on Auditory Evoked-Potentials.* International Journal of Psychophysiology, 1990. **9**(1): p. 81-84.
44. Barik, U. K. and Srinivasan, S. et al., *Electrical and optical properties of reactive DC magnetron sputtered silver oxide thin films: role of oxygen,* Thin Solid Films, 2003. **429**(1-2): p. 129-134
45. Almtoft KP, Bottiger J, Chevallier J, Schell N, *Influence of the substrate bias on the size and thermal stability of grains in magnetron-sputtered nanocrystalline Ag films* , Journal Of Materials Research, 2005, 20 (4): p. 1071-1080.
46. Huang, H. B. and Spaepen, F.*, Tensile testing of free-standing Cu, Ag and Al thin films and Ag/Cu multilayers,* Acta Materialia, 2000. **48**(12): p. 3261-3269.

47. Schmidt, S. and Grimes, **C. A.,** *Characterization of nano-dimensional thin-film elastic moduli using magnetoelastic sensors,* Sensors and Actuators A: Physical, 2001. **94**(3): p. 189-196.
48. Laugier**, M.,** *Determination of Young's modulus in vacuum-evaporated thin films of aluminium and silver,* Thin Solid Films, 1981. **75**(4): p. L17-L18.